solids

MDPI

Review

Thermal Expansion Behavior in the $A_2M_3O_{12}$ Family of Materials

Hongfei Liu [1,*], Weikang Sun [1], Zhiping Zhang [1,2], La'Nese Lovings [3] and Cora Lind [3,*]

[1] School of Physical Science and Technology, Yangzhou University, Yangzhou 225002, China; 15380378749@sina.cn (W.S.); zhiping@yzu.edu.cn (Z.Z.)
[2] Guangling College, Yangzhou University, Yangzhou 225002, China
[3] Department of Chemistry and Biochemistry, The University of Toledo, 2801 W. Bancroft St., Toledo, OH 43606, USA; lanese.lovings@rockets.utoledo.edu
* Correspondence: liuhf@yzu.edu.cn (H.L.); cora.lind@utoledo.edu (C.L.); Tel.: +86-514-87975466 (H.L.); +1-419-5301505 (C.L.)

Abstract: Over the past several decades, research on anomalous thermal expansion materials has been rapidly growing, and increasing numbers of compounds exhibiting negative thermal expansion (NTE) have been reported. In particular, compounds with formula $A_2M_3O_{12}$ have attracted considerable attention. $A_2M_3O_{12}$ family materials offer a wide range of possible compositions due to the chemical flexibility of the A and M sites. According to published research, more than half of them possess NTE properties. This paper reviews the range of physical properties displayed by materials in the $A_2M_3O_{12}$ family. Research on improving material imperfections and controlling the coefficient of thermal expansion in the $A_2M_3O_{12}$ family are systematically summarized. Finally, challenges and questions about the developments of these $A_2M_3O_{12}$ NTE compounds in future studies are also discussed.

Keywords: negative thermal expansion; scandium tungstate; hygroscopicity; phase transition; challenges

Citation: Liu, H.; Sun, W.; Zhang, Z.; Lovings, L.; Lind, C. Thermal Expansion Behavior in the $A_2M_3O_{12}$ Family of Materials. *Solids* **2021**, *2*, 87–107. https://doi.org/

Academic Editor: Guido Kickelbick
Received: 30 December 2020
Accepted: 11 February 2021
Published: 19 February 2021

1. Introduction

In recent years, the fields of microelectronics, photoelectric communications and aerospace have rapidly expanded. Materials with high-precision size are in growing demand, and dimensional stability and long lifetime of devices at different operating temperatures is of high importance. A mismatch of thermal expansion coefficients combined with a temperature variation of the materials' environment can result in thermal stress, thus leading to performance degradation or permanent damage to devices. Therefore, low, and especially near-zero expansion materials, are beneficial to improve the geometrical stabilities of these materials and devices. The discovery of negative thermal expansion (NTE) behavior in compounds provides the possibility of developing materials with controllable or near-zero thermal expansion coefficients for specific applications.

Previous research on NTE materials has focused on the following families: Metal cyanides [1–6], metal fluorides [7–16], Mn_3AN (A = Cu, Zn, Ge, Sn, Ag) [17–23], intermetallics [24–31], metal oxides including AM_2O_8 (A = Zr, Hf; M = W, Mo) [32–38], AM_2O_7 (A = Zr, Hf; M = V, P) [39–42], A_2O (A = Ag, Cu) [43–47] and $A_2M_3O_{12}$ (A = trivalent cation; M = W, Mo) [48–50]. Compared to the other families, the $A_2M_3O_{12}$ stoichiometry has received special attention because of the broad range of metals that can be incorporated into the structure. The A-site can be fully occupied by a single trivalent metal ranging in size from Al^{3+} to the smaller lanthanides, or partially substituted by most lanthanides and many transition metals, whereas the M-site is usually occupied by tungsten or molybdenum. Aliovalent substitution of both metal sites has also been reported. The wide range of compositions accessible in the $A_2M_3O_{12}$ family is unique. This paper reviews the thermal

expansion properties of the $A_2M_3O_{12}$ family with a focus on compounds displaying NTE behavior. Recent advances are discussed in detail as well as promising future prospects.

2. Positive Thermal Expansion

The $A_2M_3O_{12}$ family consists of a large number of compounds that can adopt several different structure types. The identity of the A and M site elements determines the preferred structure type which is intimately related to the thermal expansion properties of the compounds. According to the systematic research conducted by Nassau et al. [51], when the A-site is occupied by the larger lanthanides ranging from La^{3+} to Tb^{3+}, these tungstates and molybdates display positive thermal expansion. $Dy_2Mo_3O_{12}$ also belongs to this group of compounds, while $Dy_2W_3O_{12}$ does not [52,53]. The crystal structures of these positive thermal expansion $A_2M_3O_{12}$ compositions are orthorhombic in space group Pba2 or monoclinic in space group C2/c, and contain edge-shared AO_7-polyhedra, which are generally considered as an unfavorable factor for NTE behavior. For instance, Figure 1 shows the typical structure of $Gd_2Mo_3O_{12}$ [54]. Gd^{3+} is coordinated by seven oxygen atoms, while Mo^{6+} is bonded to four oxygen atoms. The GdO_7 units share common edges, causing oxygen atoms to be coordinated by three instead of two atoms. This connection mode hampers transverse vibration of oxygen atoms, the typical basis of NTE in the $A_2M_3O_{12}$ family.

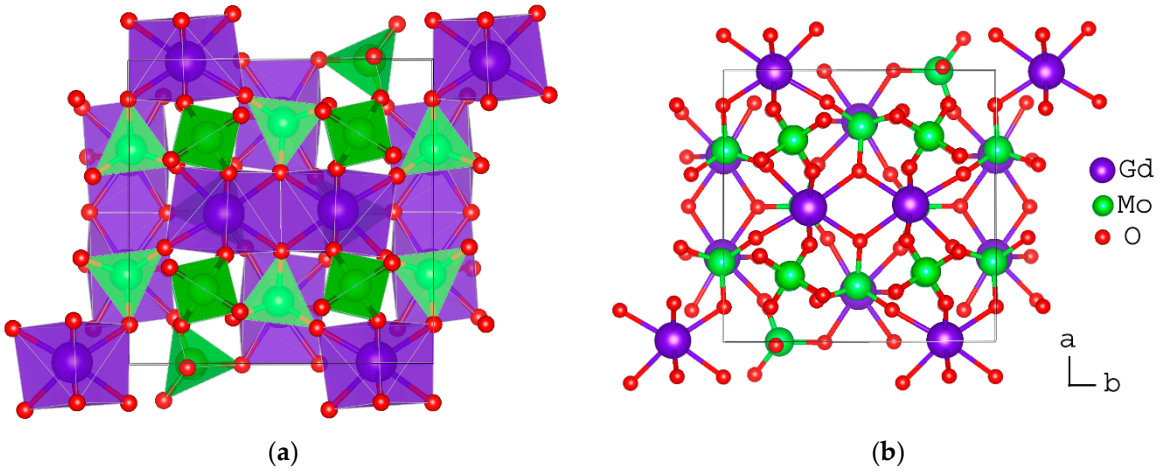

(**a**) (**b**)

Figure 1. (**a**) Crystal structure of $Gd_2Mo_3O_{12}$ and (**b**) three-fold coordinated oxygen.

3. Negative Thermal Expansion

In the field of NTE research, the $A_2M_3O_{12}$ family is also referred to as the scandium tungstate family. Scandium tungstate adopts an orthorhombic structure in the space group Pnca at all temperatures (Figure 2) [55,56]. The crystal structure is composed of a corner-sharing framework of octahedral ScO_6 and tetrahedral WO_4 units. No edge-sharing is observed, in contrast to the $Gd_2Mo_3O_{12}$-type structure discussed earlier. As the bond lengths of Sc-O and W-O show little change with temperature, the global expansion behavior is dominated by transverse motions of the corner-sharing oxygens. Diffraction data demonstrate that these vibrations give rise to a reduction of the Sc-O-W bond angle and a shortening of the next-nearest neighbor distances on a microscopic level and macroscopic NTE of the material [55]. The resulting rocking motions of the polyhedral building blocks are accompanied by some distortion of the polyhedra. Larger A-site cations can more readily accompany these distortions, and thus favor more significant NTE [57].

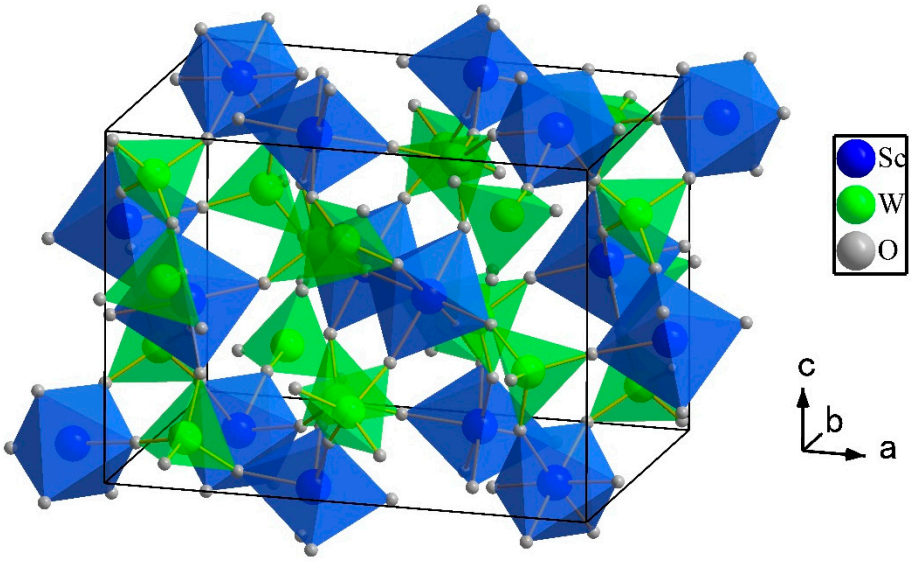

Figure 2. Crystal structure of orthorhombic $Sc_2W_3O_{12}$: blue: ScO_6 octahedra; green: WO_4 tetrahedra.

When the A-site is occupied by Ho^{3+}, Y^{3+}, Er^{3+}, Tm^{3+}, Yb^{3+}, Lu^{3+}, Sc^{3+}, In^{3+}, Fe^{3+}, Cr^{3+}, Ga^{3+} or Al^{3+}, almost all tungstates and molybdates have been reported to form stable compounds that adopt the same structure as $Sc_2W_3O_{12}$ and display NTE behavior [50,58]. Some compositions can undergo a phase transition from the orthorhombic NTE phase at high temperatures to a denser monoclinic positive thermal expansion (PTE) structure at low temperatures [59]. This phase transition can also be induced by applying pressure, which will be discussed later in this review.

Many attempts to synthesize single phase $Fe_2W_3O_{12}$ and $Cr_2W_3O_{12}$ using different approaches, such as solid-state, co-precipitation and sol-gel methods failed to obtain single phase $Fe_2W_3O_{12}$ and $Cr_2W_3O_{12}$ [60,61]. This is mainly because both $Fe_2W_3O_{12}$ and $Cr_2W_3O_{12}$ are metastable phases, which decompose to $FeWO_4$ or $CrWO_4$ and WO_3 during heating. Other researchers reported successful synthesis, but did not display diffraction data [62,63] or displayed data that cannot exclude the presence of an amorphous component or small impurity phases [64,65]. Recently, Yang et al. fabricated Mo-doped single-phase $Fe_2W_3O_{12}$ using rapid solid-state reactions with excess MoO_3 [66]. $Fe_2W_3O_{12}$ still showed positive thermal expansion after the monoclinic-to-orthorhombic phase transition with a coefficient of thermal expansion of 1.35×10^{-6} °C^{-1} (445–600 °C) as measured by dilatometry. $Ga_2Mo_3O_{12}$ is another difficult to synthesize composition, which can only be obtained by non-hydrolytic sol-gel chemistry [67], and remains monoclinic with positive expansion until its decomposition temperature around 650 °C.

It is generally accepted that the coefficient of thermal expansion (CTE) is related to the size of the A-site trivalent cation, and that it decreases with increasing size of the A-site ion. To date, Y^{3+} has the largest ionic radius (0.90 Å) of the materials adopting the orthorhombic Pnca structure, and $Y_2Mo_3O_{12}$ and $Y_2W_3O_{12}$ display intrinsic linear thermal expansion coefficients of -9.36×10^{-6} °C^{-1} [68] and -7.0 to -7.4×10^{-6} °C^{-1} [69,70], respectively, in the temperature range of 200 to 800 °C. Only $Ho_2Mo_3O_{12}$ has been reported to possess an even larger negative intrinsic α_l value of -11.56×10^{-6} °C^{-1} [71], although several rare earth molybdates and tungstates show similar magnitudes of linear NTE [52,68,72]. These A-site cations are very similar in size to Y^{3+}. However, many $A_2M_3O_{12}$ compounds with large A-site ions possess the ability to absorb water, which inhibits the NTE behavior of the materials.

3.1. Mechanism of Negative Thermal Expansion in the $A_2M_3O_{12}$ Family

Several excellent reviews discussing the origins of NTE in different classes of compounds have recently been published [73,74]. Both intrinsic structural features, and structural or magnetic phase transitions, can contribute to the observed behavior. The negative

thermal expansion observed in Pnca-$A_2M_3O_{12}$ compounds is categorized as intrinsic structural NTE. It arises from transverse vibrational motions of the 2-coordinated oxygens. In materials that contain mostly 2-coordinate linkers in approximately linear coordination, these vibrations result in concerted bending and torsional motions that reduce the distances between next-nearest neighbor metal centers. When these reductions outweigh the bond expansion due to longitudinal vibrations, NTE results. This visual concept for explaining NTE behavior was introduced early on for ZrW_2O_8 [34], and has since been applied to many other NTE materials that possess corner-sharing polyhedral networks. Other authors refer to it as the "tension effect" to indicate that the vibrations result in forces that cause rocking motions of the polyhedral building blocks [75,76]. In physics terms, these lattice vibrations are described as phonon modes, and both optical and acoustic transverse phonon modes with negative Grüneisen parameters can contribute to NTE, which is observed when the overall Grüneisen parameter is negative over an extended temperature range. If these modes occur without distortion of the polyhedra, they are referred to as rigid unit modes (RUMs), whereas modes in solids that show some changes within the polyhedra are often called quasi rigid unit modes (QRUMs) [37,77]. Tao and Sleight showed that the $A_2M_3O_{12}$ family can only support QRUMs [78]. Evidence for transverse phonon modes in NTE materials was obtained by heat capacity and phonon density of states measurements [38,79]. Theoretical calculations have also been used to elucidate NTE mechanisms [80,81].

3.2. Hygroscopicity in the $A_2M_3O_{12}$ Family

When the A-site is occupied by the smaller rare earth elements or pseudo-lanthanides, more specifically, Ho^{3+}, Y^{3+}, Er^{3+}, Tm^{3+}, Yb^{3+} and Lu^{3+}, the $A_2M_3O_{12}$ materials display strong NTE and remain orthorhombic to the lowest temperatures studied [68,69,71,72,82–84]. The large negative CTEs are attributed to the large ionic radii. However, the large ionic radii also cause hygroscopicity, as this gives rise to the emergence of microchannels accessible to water in the crystal structure [82,84,85]. Moisture from the atmosphere results in formation of trihydrates, with the water molecules interacting with the structure via strong hydrogen bonds. The presence of water and hydrogen bonding networks weakens or in most cases eliminates NTE behavior [86], and removal of the water is necessary to reclaim the NTE properties. Marinkovic et al. researched NTE and hygroscopicity of $Y_2Mo_3O_{12}$ in detail, and found that the microchannels in the lattice are large enough for water molecules to enter freely and play a part in causing partial amorphization of $Y_2Mo_3O_{12}$ upon hydration. A summary of CTEs and the corresponding temperature ranges for these hygroscopic materials can be found in Table 1.

Table 1. Intrinsic coefficients of thermal expansion (CTEs) of hygroscopic materials in the $A_2M_3O_{12}$ family based on variable temperature diffraction data.

Compound	α_1 ($\times 10^{-6}$ °C^{-1})	T Range (°C)	Ref.
$Y_2Mo_3O_{12}$	−9.36 [1]	25–800	[68]
$Y_2W_3O_{12}$	−7.34 [1]	200–800	[72]
$Dy_2W_3O_{12}$	−8.60	150–500	[52]
$Ho_2Mo_3O_{12}$	−11.56	200–700	[71]
$Ho_2W_3O_{12}$	−6.97	200–600	[83]
$Er_2Mo_3O_{12}$	−7.56 [1]	25–800	[68]
$Er_2W_3O_{12}$	−6.74 [1]	200–800	[72]
$Tm_2Mo_3O_{12}$	−4.04	200–800	[71]
$Tm_2W_3O_{12}$	−3.99	200–800	[71]
$Lu_2Mo_3O_{12}$	−6.02 [1]	25–800	[68]
$Lu_2W_3O_{12}$	−6.18 [1]	200–800	[72]
$Yb_2Mo_3O_{12}$	−6.04 [1]	25–800	[68]
$Yb_2W_3O_{12}$	−6.38 [1]	200–800	[72]

[1] Collected under vacuum.

Ample research has been performed with the materials in Table 1 to synthesize controllable thermal expansion materials that are less hygroscopic by chemical modification. Substitution of small amounts of Al, Cr, Fe or Sc generally did not eliminate water uptake [87–93], while lanthanide poor compositions showed less tendency to absorb moisture. For Al, Cr and Fe, hygroscopicity was overcome for compositions that resulted in formation of the denser monoclinic PTE phase, which is less favorable for water incorporation. For Sc, a non-hygroscopic material was obtained for $Sc_{1.75}Y_{0.25}W_3O_{12}$. A length change of -7.13×10^{-6} °C^{-1} was detected by dilatometry. Substitution of a larger rare earth ion that favors edge-shared structures has also been explored [88,94–97]. In this context, we previously prepared $Y_{2-x}Ce_xW_3O_{12}$ solid solutions to adjust the magnitude of the CTE and to overcome the hygroscopicity of $Y_2W_3O_{12}$ [97]. Results showed that moisture absorption was no longer observed for $x \geq 1.5$ at room temperature, however, compositions with $x \geq 0.5$ also showed the presence of the denser monoclinic C2/c structure, with coexistence of the orthorhombic and monoclinic phases for x = 0.5. Dilatometer measurements still showed NTE for compositions up to $Y_{0.25}Ce_{1.75}W_3O_{12}$ (-0.82×10^{-6} °C^{-1}), suggesting that such monoclinic ceramics could be promising near-zero thermal expansion materials. Double ion substitution such as $(LiMg)^{3+}$ has also been implemented to reduce hydrophilicity in $Y_2Mo_3O_{12}$ by Cheng et al. [98]. The hygroscopicity of the sample was eventually eliminated, but the thermal expansion of the material increased with the addition of $(LiMg)^{3+}$. In addition to the method of ion-doping, Liu et al. chose C_3N_4 as a coating material to protect $Y_2Mo_3O_{12}$ from water exposure [99]. This successfully prevented hydration, and retained similar expansion coefficients.

3.3. Non-Hygroscopic $A_2M_3O_{12}$ Compositions with Corner-Shared Networks

When the A-site is occupied by Sc^{3+}, In^{3+}, Fe^{3+}, Cr^{3+}, Ga^{3+} and Al^{3+}, $A_2M_3O_{12}$ compositions do not absorb water molecules from air. Most of these materials undergo a reversible temperature-induced phase transition from a low temperature monoclinic structure in the space group $P2_1/a$ to the orthorhombic $Sc_2W_3O_{12}$ structure in the space group Pnca at higher temperatures. Exceptions are $Sc_2W_3O_{12}$, which remains orthorhombic to the lowest temperatures investigated [55], and $Ga_2Mo_3O_{12}$, which decomposes to the binary oxides before transforming to the orthorhombic phase [67]. Only Pnca-$A_2M_3O_{12}$ materials exhibit notable negative thermal expansion. In general, the phase transition temperature increases with increasing electronegativity of the A-site ion. This can be attributed to the fact that A-site cations with higher electronegativity reduce the partial negative charge of the oxygen atoms and weaken the repulsive forces between them, which stabilizes the denser monoclinic structure to higher temperatures. The transition temperature can be determined by refinement of diffraction data, Raman spectroscopy, dilatometry or thermal analysis. The temperatures of the monoclinic to orthorhombic phase change are summarized in Table 2.

The exact relationship between the monoclinic and orthorhombic structures was demonstrated for $Sc_2Mo_3O_{12}$ by Evans et al. [59]. This material adopts a monoclinic structure below −93 °C that displays PTE with an expansion coefficient of 2.19×10^{-5} °C^{-1}. Above −93 °C, orthorhombic $Sc_2Mo_3O_{12}$ shows NTE with a linear expansion coefficient of -6.3×10^{-6} °C^{-1}. Figure 3 shows the two crystal structures of $Sc_2Mo_3O_{12}$ and their crystallographic relationship, which is given by $\mathbf{a_m} \approx -\mathbf{b_o} + \mathbf{c_o}$, $\mathbf{b_m} \approx -\mathbf{a_o}$, and $\mathbf{c_m} \approx -2\mathbf{c_o}$.

Scandium tungstate is the only non-hygroscopic compound that does not undergo a phase transition to the lowest temperatures investigated [55]. It shows stable NTE performance over a wide temperature range from −263 °C to 800 °C and is non-hygroscopic in air. Because of this, it is considered to be one of the most promising NTE compounds in the $A_2M_3O_{12}$ family. $Sc_2Mo_3O_{12}$ [59] and $Al_2W_3O_{12}$ [101] possess phase transition temperatures that are below room temperature, while the rest of the non-hygroscopic phase change materials undergo the transition at temperatures between 200 and 500 °C [66,100–104]. High phase transition temperatures are considered undesirable for fabricating devices, and approaches that allow lowering of the transition temperatures would be beneficial. To date, this has mainly been attempted by doping with different A-site elements, which

showed that controlling the phase transition temperature to meet specific environments is promising and feasible [100,103,104].

Table 2. Phase transition temperatures and CTEs of orthorhombic phases of compounds in the $A_2M_3O_{12}$ (A = Al^{3+}, Sc^{3+}, Cr^{3+}, Fe^{3+}, Ga^{3+} and In^{3+}) family. Intrinsic α_l values based on variable temperature diffraction data are reported unless indicated otherwise. NR = not reported.

Compound	T_{PT} (°C)	α_l ($\times 10^{-6}$ °C^{-1})	T Range	Ref.
$Al_2Mo_3O_{12}$	200	2.32	250–650	[100]
$Al_2W_3O_{12}$	−6	1.51	20–800	[69,101]
$Sc_2Mo_3O_{12}$	−93	−2.11	−73–27	[59]
$Sc_2W_3O_{12}$	NR	−2.20	−263–177	[55]
$Cr_2Mo_3O_{12}$	403	0.67	420–740	[100]
$Fe_2Mo_3O_{12}$	512	1.72	550–740	[100]
$Fe_2W_3O_{12}$	414–445	1.35 [1]	445–600	[66]
$Ga_2W_3O_{12}$	NR	−5 [1]	NR	[58]
$In_2Mo_3O_{12}$	335	−1.85	370–760	[102]
$In_2W_3O_{12}$	250	−3.00 [1]	277–700	[103]

[1] Dilatometer data.

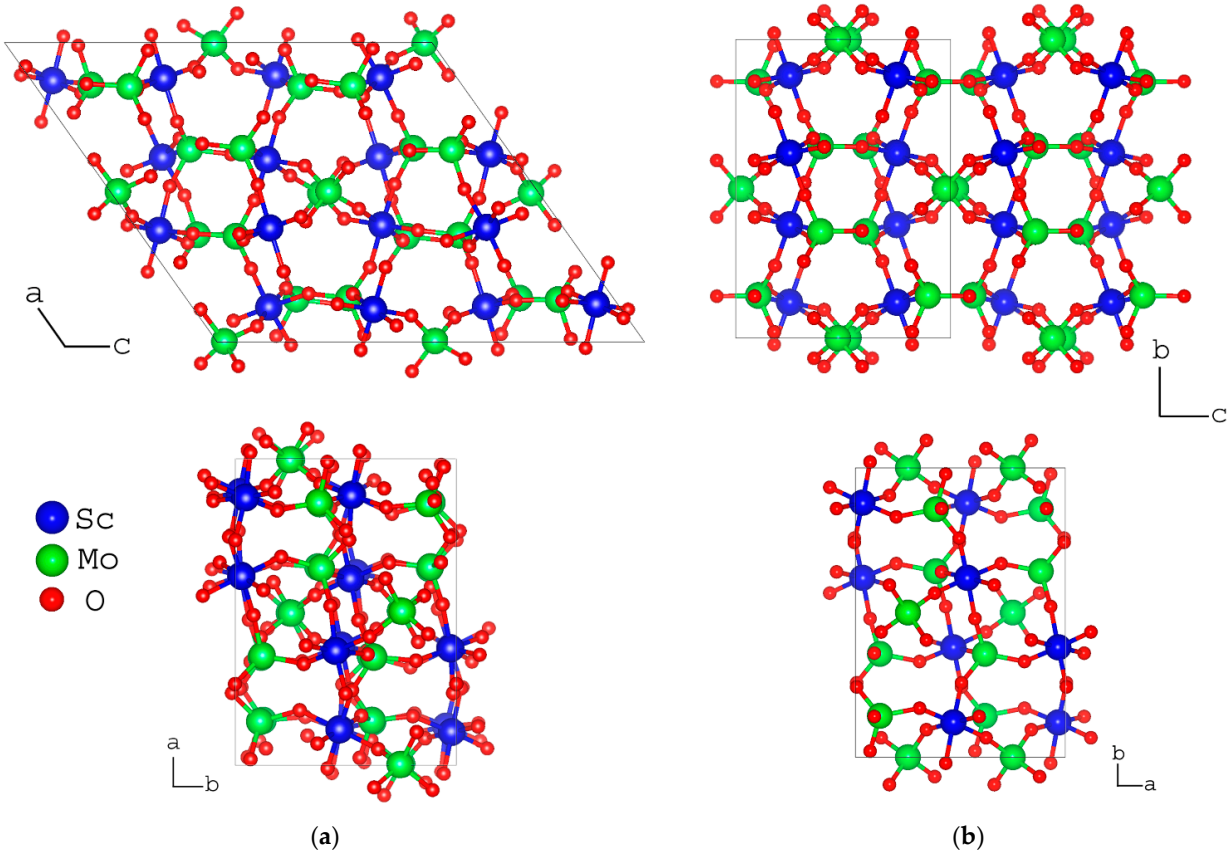

(**a**) (**b**)

Figure 3. Crystal structures of (**a**) monoclinic and (**b**) orthorhombic $Sc_2Mo_3O_{12}$.

3.3.1. Single Ion Substitution

Single ion substitution can be used to improve performance in $A_2M_3O_{12}$ NTE compounds that display high phase transition temperatures (A = Al, In, Cr, Fe; M = W and Mo). This has been applied to solid solutions to tune phase transition temperatures in the 200 to 500 °C range [100,104]. However, from an applications point of view, suppressing the phase transition temperature to room temperature or below is desirable. This can mainly be achieved by incorporation of A-site cations with low electronegativity, which is known

to lower the phase transition temperature [101]. In our previous work, we prepared solid solutions of $In_{2-x}Sc_xW_3O_{12}$ ($0 \leq x \leq 2$) using solid state reaction methods to reduce the phase transition temperature of $In_2W_3O_{12}$ [103]. Sc^{3+} was shown to effectively replace In^{3+}, and the monoclinic-to-orthorhombic phase transition temperature was shifted from 248 °C to 47 °C for x = 1. The average linear thermal expansion coefficient of $InScW_3O_{12}$ determined by dilatometry is -7.13×10^{-6} °C^{-1} in the temperature range 58 to 700 °C. The obtained thermal expansion curve for this sample is shown in Figure 4a. We have also prepared $AlScMo_3O_{12}$ by non-hydrolytic sol-gel routes [105], and found that it remains orthorhombic to −173 °C, but approaches the phase transition to the monoclinic structure at that temperature. The thermal expansion curve for this sample is shown in Figure 4b.

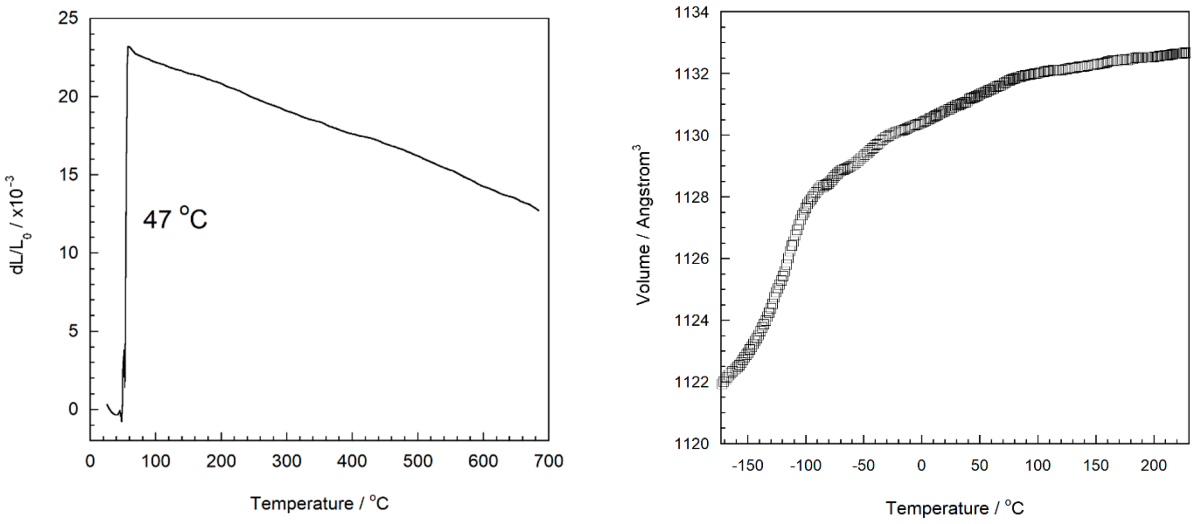

Figure 4. (**a**) Expansion curve of $InScW_3O_{12}$ obtained by dilatometry and (**b**) unit cell volume of $AlScMo_3O_{12}$.

Wu et al. synthesized $Ln_{2-x}Cr_xMo_3O_{12}$ (Ln = Er and Y) and showed via differential scanning calorimetry that the phase transition of $Cr_2Mo_3O_{12}$ could be suppressed from 400 to 197 °C by substitution of 10% Er [93]. Similarly, Li et al. showed that with increasing Y^{3+} content in the solid solution $Fe_{2-x}Y_xMo_3O_{12}$, the phase transition temperature could be decreased significantly, with $Fe_{1.5}Y_{0.5}Mo_3O_{12}$ showing the transition below −170 °C [87]. Substitution of $Fe_{2-x}Ln_xMo_3O_{12}$ by other lanthanides (Ln = Er, Lu, Yb) resulted in orthorhombic materials at or below room temperature [87,90,91]. These reports demonstrate that single ion substitution can successfully broaden the temperature range in which the orthorhombic NTE phase is stable. However, these compounds become hygroscopic even after incorporation of small quantities of lanthanides, making substitution by Sc^{3+} most attractive. Work on single ion doping on the M-site to reduce the phase transition temperature is rare. Shen et al. prepared $Al_2Mo_{3-x}W_xO_{12}$ solid solutions to adjust the coefficient of thermal expansion of $Al_2Mo_3O_{12}$ and found a less significant reduction of the phase transition temperature of $Al_2Mo_{3-x}W_xO_{12}$ with increasing W^{6+} content [106]. Liu et al. later suggested that this could be explained by the lower electronegativity of W^{6+} compared to Mo^{6+}, which is consistent with the effect of the electronegativity of the A^{3+} cation on the transition temperatures [107]. Table 3 gives an overview of selected mono-substituted compounds for which phase transition temperatures and expansion coefficients have been reported.

Table 3. Variation in phase transition temperature (T_{PT}) by single A-site doping and corresponding intrinsic linear CTEs determined from variable temperature diffraction data, unless otherwise indicated. Elements for each site are listed in alphabetical order.

Compound	T_{PT} (°C)	α_l ($\times 10^{-6}$ °C^{-1})	Ref.	Compound	T_{PT} (°C)	α_l ($\times 10^{-6}$ °C^{-1})	Ref.
$Al_2Mo_3O_{12}$	200	2.32	[100]	$Cr_{1.8}Er_{0.2}Mo_3O_{12}$	197	0.47	[93]
$Al_{1.8}Cr_{0.2}Mo_3O_{12}$	214	NR	[100]	$Cr_{0.2}Er_{1.8}Mo_3O_{12}$	<RT	−4.20	[93]
$Al_{1.4}Cr_{0.6}Mo_3O_{12}$	244	2.37	[100]	$Cr_{1.4}Fe_{0.6}Mo_3O_{12}$	441	0.97	[100]
$AlCrMo_3O_{12}$	284	1.85	[100]	$CrFeMo_3O_{12}$	465	1.21	[100]
$Al_{0.6}Cr_{1.4}Mo_3O_{12}$	328	1.38	[100]	$Cr_{0.6}Fe_{1.4}Mo_3O_{12}$	484	1.40	[100]
$Al_{0.2}Cr_{1.8}Mo_3O_{12}$	374	NR	[100]	$Cr_{1.7}Sc_{0.3}Mo_3O_{12}$	276	−4.34 [1]	[108]
$Al_{1.8}Fe_{0.2}Mo_3O_{12}$	240	NR	[100]	$Cr_{1.5}Sc_{0.5}Mo_3O_{12}$	204	0.99	[109]
$Al_{1.6}Fe_{0.4}Mo_3O_{12}$	273	NR	[100]	$Cr_{1.4}Sc_{0.6}Mo_3O_{12}$	177	−2.81 [1]	[108]
$Al_{1.4}Fe_{0.6}Mo_3O_{12}$	305	3.40	[100]	$Cr_{1.1}Sc_{0.9}Mo_3O_{12}$	149	−5.87 [1]	[108]
$Al_{1.2}Fe_{0.8}Mo_3O_{12}$	399	NR	[100]	$Cr_{0.8}Sc_{1.2}Mo_3O_{12}$	65	−4.57 [1]	[108]
$AlFeMo_3O_{12}$	369	3.29	[100]	$Cr_{0.7}Sc_{1.3}Mo_3O_{12}$	<RT	−0.47	[109]
$Al_{0.8}Fe_{1.2}Mo_3O_{12}$	399	NR	[100]	$Cr_{0.6}Sc_{1.4}Mo_3O_{12}$	<RT	−11.17 [1]	[108]
$Al_{0.6}Fe_{1.4}Mo_3O_{12}$	430	NR	[100]	$Cr_{0.5}Sc_{1.5}Mo_3O_{12}$	<RT	−0.51	[109]
$Al_{0.4}Fe_{1.6}Mo_3O_{12}$	457	NR	[100]	$Cr_{1.8}Yb_{0.2}Mo_3O_{12}$	204	1.13	[92]
$Al_{0.2}Fe_{1.8}Mo_3O_{12}$	484	NR	[100]	$Cr_{0.4}Yb_{1.6}Mo_3O_{12}$	<RT	−1.69	[92]
$Al_{1.5}Ga_{0.5}Mo_3O_{12}$	400	4.5	[110]	$Cr_{0.2}Yb_{1.8}Mo_3O_{12}$	<RT	−4.73	[92]
$AlGaMo_3O_{12}$	300	1.9	[110]	**$Fe_2Mo_3O_{12}$**	512	1.72	[100]
$Al_{0.5}Ga_{1.5}Mo_3O_{12}$	250	0.1	[110]	$Er_{0.2}Fe_{1.8}Mo_3O_{12}$	344	NR	[90]
$Al_{1.3}Sc_{0.7}Mo_3O_{12}$	<RT	3.06	[111]	$Fe_{1.5}Lu_{0.5}Mo_3O_{12}$	400	2.31	[91]
$AlScMo_3O_{12}$	<−173	3.60	[105]	$FeLuMo_3O_{12}$	<RT	0.99	[91]
$Al_{0.3}Sc_{1.7}Mo_3O_{12}$	<RT	−0.73	[111]	$Fe_{0.3}Lu_{1.7}Mo_3O_{12}$	<RT	−3.13	[91]
$Al_{1.8}Yb_{0.2}Mo_3O_{12}$	157	9.5 [1]	[88]	$Fe_{1.6}Sc_{0.4}Mo_3O_{12}$	376	−6.25 [1]	[112]
$Al_{1.6}Yb_{0.4}Mo_3O_{12}$	<RT	5.74 [1]	[88]	$Fe_{1.2}Sc_{0.8}Mo_3O_{12}$	241	1.17	[113]
$Al_{0.4}Yb_{1.6}Mo_3O_{12}$	<RT	−5.5 [1]	[88]	$Fe_{0.8}Sc_{1.2}Mo_3O_{12}$	109	−4.18 [1]	[112]
$Al_{0.2}Yb_{1.8}Mo_3O_{12}$	<RT	−9.1 [1]	[88]	$Fe_{0.7}Sc_{1.3}Mo_3O_{12}$	112	0.09	[113]
$Al_2Mo_{2.5}W_{0.5}O_{12}$	127	4.85 [1]	[106]	$Fe_{0.4}Sc_{1.6}Mo_3O_{12}$	<RT	−0.83	[113]
$Al_2Mo_{2.5}W_{0.5}O_{12}$	118	5.20 [1]	[106]	$Fe_{1.8}Y_{0.2}Mo_3O_{12}$	348	NR	[87]
$Al_2Mo_{2.5}W_{0.5}O_{12}$	101	4.00 [1]	[106]	**$In_2Mo_3O_{12}$**	335	−1.85	[102]
$Al_2Mo_{2.5}W_{0.5}O_{12}$	71	0.80 [1]	[106]	$In_{1.7}Sc_{0.3}Mo_3O_{12}$	271	−8.41 [1]	[114]
$Al_2Mo_{2.5}W_{0.5}O_{12}$	NR	0.05 [1]	[106]	$In_{1.4}Sc_{0.6}Mo_3O_{12}$	205	−6.32 [1]	[114]
$Al_2W_3O_{12}$	−6	1.51	[69]	$In_{1.1}Sc_{0.9}Mo_3O_{12}$	137	−5.83 [1]	[114]
$Al_{1.9}Ga_{0.1}W_3O_{12}$	21	NR	[115]	$In_{0.8}Sc_{1.2}Mo_3O_{12}$	77	−11.27 [1]	[114]
$Al_{1.8}Ga_{0.2}W_3O_{12}$	60	NR	[115]	$In_{0.5}Sc_{1.5}Mo_3O_{12}$	<RT	−5.08 [1]	[114]
$Al_{1.7}Ga_{0.3}W_3O_{12}$	91	NR	[115]	**$In_2W_3O_{12}$**	250	−3.00 [1]	[103]
$Al_{1.6}Ga_{0.4}W_3O_{12}$	108	NR	[115]	$ErInW_3O_{12}$	135	NR	[50]
$Al_{0.7}In_{1.3}W_3O_{12}$	118	NR	[116]	$In_{1.9}Sc_{0.1}W_3O_{12}$	224	−5.29 [1]	[103]
$Al_{0.5}In_{1.5}W_3O_{12}$	181	NR	[116]	$In_{1.7}Sc_{0.3}W_3O_{12}$	168	NR	[117]
$Al_{1.9}Sc_{0.1}W_3O_{12}$	−35	~0.2 [1]	[115]	$In_{1.5}Sc_{0.5}W_3O_{12}$	147	−1.28 [1]	[103]
$Al_{1.8}Sc_{0.2}W_3O_{12}$	−60	~0.6 [1]	[115]	$In_{1.4}Sc_{0.6}W_3O_{12}$	76	NR	[117]
$Al_{1.7}Sc_{0.3}W_3O_{12}$	−98	~1.4 [1]	[115]	$In_{1.1}Sc_{0.9}W_3O_{12}$	<RT	−5.35 [1]	[117]
$Al_{1.6}Sc_{0.4}W_3O_{12}$	<−150	~1.4 [1]	[115]	$In_{0.8}Sc_{1.2}W_3O_{12}$	<RT	NR	[117]
$Al_{0.8}Sc_{1.2}W_3O_{12}$	<RT	1.21	[118]	**$Sc_2Mo_3O_{12}$**	−93	−2.11	[59]
$Al_{0.5}Sc_{1.5}W_3O_{12}$	<RT	−0.32	[118]	**$Sc_2W_3O_{12}$**	<−263	−2.20	[55]
$Al_{0.3}Sc_{1.7}W_3O_{12}$	<RT	−0.93	[118]	**$Y_2Mo_3O_{12}$**	<−263	−9.02	[119]
$Cr_2Mo_3O_{12}$	403	0.67	[100]	**$Y_2W_3O_{12}$**	<−258	−7.0	[49]

[1] Dilatometer data.

Figure 5 shows the relationship between average A-site electronegativity and phase transition temperature for $A_{2-x}A'_xM_3O_{12}$ compositions. Compounds with reported transition temperatures below room temperature are marked by name. The molybdates generally follow a linear trend, with the exception of $AlScMo_3O_{12}$ and $Fe_{1.5}Y_{0.5}Mo_3O_{12}$. These compounds both contain two A-site cations with a significant size difference, which according to Truitt et al. can result in the suppression of the phase transition temperature [105]. Inter-

estingly, the behavior of the tungstates is more varied, resulting in two distinct branches with some scattered values in-between. It is worth noting that all compounds on the lower branch contain aluminum as one of the A-site cations, while all compositions on the upper branch contain indium. The two reported $Al_{2-x}In_xW_3O_{12}$ compositions contribute the datapoints between the two lines. The formation of these two branches is related to the large difference in phase transition temperature for $Al_2W_3O_{12}$ and $Inl_2W_3O_{12}$ combined with the very similar electronegativities of aluminum and indium.

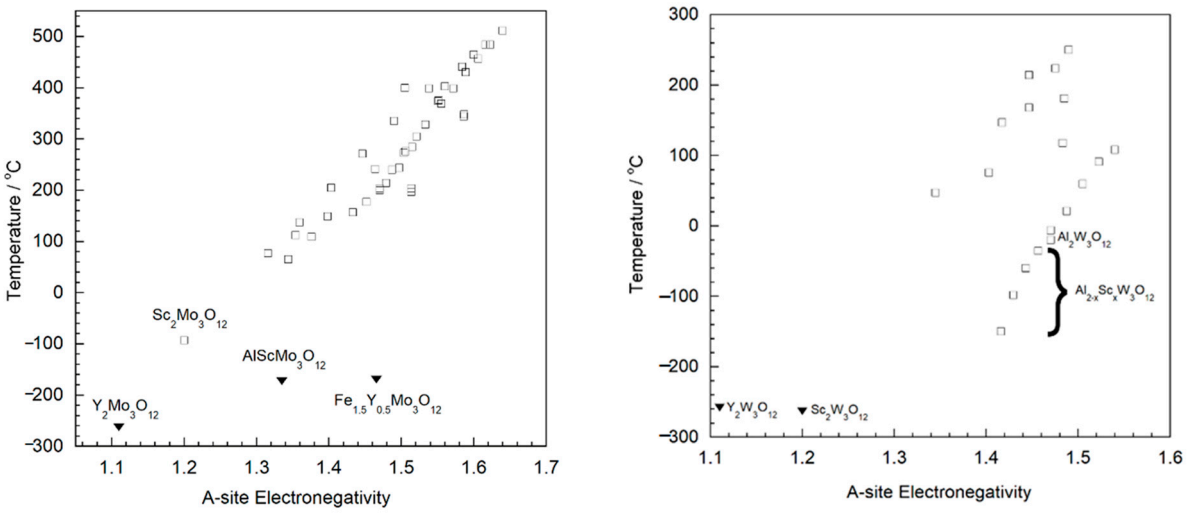

(**a**) (**b**)

Figure 5. Monoclinic to orthorhombic phase transition temperatures for monosubstituted $A_2M_3O_{12}$ compositions as a function of average A-site electronegativity for (**a**) molybdates and (**b**) tungstates. Triangles represent compounds that remained orthorhombic to the lowest temperatures investigated.

3.3.2. Aliovalent Substitutions

Considerable work has been performed on single ion substitution with cations of the same charge (trivalent A-site or hexavalent M-site cations). In addition, both the A- and M-site of $A_2M_3O_{12}$ can be substituted by a number of aliovalent cations. The guiding principles of single or double ion doping to reduce the phase transition temperature of $A_2M_3O_{12}$ materials all center around choosing A-site cations with lower electronegativity. Lower electronegativity reduces the ability of the A-site cations to attract surrounding electrons, causing an increase of the partial negative charges on oxygen. The enhanced oxygen-oxygen repulsion favors the less dense orthorhombic structure, in which these atoms are separated by a larger distance. Therefore, phase transitions require less energy and occur at lower temperatures.

Aliovalent doping requires double substitution to maintain charge balance. In all cases, the A-site is at least partially occupied by a tetravalent atom (Zr^{4+}, Hf^{4+}). The extra positive charge can either be balanced by an A-site divalent metal (Mg^{2+}, Mn^{2+}, also partial substitution by Zn^{2+}) [120–129], or by partial substitution of the M-site with a pentavalent atom (P^{5+}, V^{5+}) [130–133]. The earliest reports of such substitutions were $Zr_2MP_2O_{12}$ and $Hf_2MP_2O_{12}$, which were shown to be isostructural to $Sc_2W_3O_{12}$ and possess NTE by Evans et al. [58,134]. These materials remain orthorhombic to the lowest temperatures studied, and display intrinsic NTE with α_l values of -4 to -5×10^{-6} °C^{-1} [58,135,136].

The first aliovalent double substitution of the A-site was accomplished when Suzuki et al. synthesized $HfMgW_3O_{12}$ [124]. The equivalent Zr- and Mo-substituted compositions were reported as well [126,137]. In contrast to $Zr_2MP_2O_{12}$ and $Hf_2MP_2O_{12}$, these materials adopt a cation-ordered structure in the space group $Pna2_1$ [138] and show small negative to small positive intrinsic α_l values [122,124,126,129,138,139]. Evidence for a monoclinic phase at low temperatures has been observed as well [127], and some authors

detected hygroscipic behavior [140,141]. Significant ion conductivity was reported as well [142]. For the molybdates, Mg^{2+} can also be replaced by Mn^{2+}, which enhances the NTE of the orthorhombic phase slightly, but also results in formation of a monoclinic phase with PTE below 90 °C [125]. Partial substitution by Zn^{2+} (up to $ZrMg_{0.65}Zn_{0.35}Mo_3O_{12}$ [143] and $HfMg_{0.5}Zn_{0.5}Mo_3O_{12}$ [120]) has also been achieved, and also increases the phase transition temperature to the monoclinic structure. Based on the consideration of valence balance, partial substitution of a trivalent A-site cation with a +2/+4 cation combination has also been explored to further tune the properties of $A_2M_3O_{12}$ compounds. These include (ZrMg) doping of $Al_2W_3O_{12}$ [140], $Cr_2Mo_3O_{12}$ [123] and $In_2Mo_3O_{12}$ [144] as well as (HfMg) doping of $Al_2W_3O_{12}$ [145], $Fe_2Mo_3O_{12}$ [146] and $In_2Mo_3O_{12}$ [147,148]. Similarly to single ion substitution, the lower electronegativity of Mg and Zr contributes to the reduction in phase transition temperature.

Another interesting set of materials has been created by matching partial substitution of the A-site by Zr^{4+} or Hf^{4+} with the equivalent amount of P^{5+} or V^{5+} incorporation on the M-site. The majority of investigations focused on Sc^{3+} as the trivalent A-site cation [131–133,149–151], but materials containing Mn^{3+}, Cr^{3+}, Fe^{3+} and Y^{3+} have also been reported [130,152–154]. Phase transition temperatures considerably below room temperature were observed for many materials. In addition, several compositions exhibit intense photoluminescence. Relevant expansion coefficients and phase transition temperatures (where investigated) are summarized in Table 4.

Table 4. Phase transition temperatures (T_{PT}) and corresponding linear thermal expansion coefficients determined from diffraction data for aliovalently substituted $A_2M_3O_{12}$ materials.

Compound	T_{PT} (°C)	α_l ($\times 10^{-6}$ °C^{-1})	T Range	Ref.
$Zr_2MoP_2O_{12}$	<−264	−4.46	−151–123	[136]
$Hf_2MoP_2O_{12}$	NR	−4 [1]	NR	[58]
$Zr_2WP_2O_{12}$	<−213	−4.70	−213–27	[135]
$Hf_2WP_2O_{12}$	NR	−5 [1]	NR	[58]
$MgZrMo_3O_{12}$	−126	0.13	25–450	[138]
$MgHfMo_3O_{12}$	−98	1.02	25–740	[126,127]
$MgZrW_3O_{12}$	NR	−1.15 [1]	167–698	[140]
$MgHfW_3O_{12}$	<−193	1.18	−193–300	[141]
$MnZrMo_3O_{12}$	90	−2.8	100–500	[128]
$MnHfMo_3O_{12}$	75	−2.46	200–300	[125]
$Mg_{0.65}Zn_{0.35}ZrMo_3O_{12}$	−20	NR	NA	[143]
$Mg_{0.5}Zn_{0.5}HfMo_3O_{12}$	50	−0.11 [1]	100–400	[120]
$Al_{1.8}(MgZr)_{0.1}W_3O_{12}$	−43	1.61 [1]	21–770	[140]
$Al_{1.6}(MgZr)_{0.2}W_3O_{12}$	−70	NR	NA	[140]
$Al_{1.4}(MgZr)_{0.3}W_3O_{12}$	<−160	2.34 [1]	21−774	[140]
$Cr_{1.5}(MgZr)_{0.75}Mo_3O_{12}$	250	NR	NA	[123]
$Cr_{0.3}(MgZr)_{0.85}Mo_3O_{12}$	<−170	0.62	127–727	[123]
$Fe_{0.6}(MgZr)_{0.7}Mo_3O_{12}$	67	NR	NA	[146]
$Fe_{0.4}(MgZr)_{0.8}Mo_3O_{12}$	<−169	2.02	127–727	[146]
$In_{0.5}(MgZr)_{0.75}Mo_3O_{12}$	82	−0.16	100–500	[144]
$In(MgHf)_{0.5}Mo_3O_{12}$	152	−0.4	225–650	[147]
$ZrFeMo_2VO_{12}$	~32	0.68	150–300	[130]
$ZrScMo_2VO_{12}$	~−190	−2.19	25–500	[133]
$ZrScW_2PO_{12}$	−199	−1.75	25–600	[132]
$HfScMo_2VO_{12}$	<−123	−2.11	25–557	[149]
$HfScW_2PO_{12}$	NR	−1.27	25–1000	[131]
$Zr_{0.3}Sc_{1.7}Mo_{2.7}V_{0.3}O_{12}$	−140	−1.53	25–485	[151]
$CrSc_{0.5}Zr_{0.5}Mo_{2.5}V_{0.5}O_{12}$	~−55	1.29	−41–299	[153]
$Cr_{0.5}ScZr_{0.5}Mo_{2.5}V_{0.5}O_{12}$	<−192	0.95	−192–299	[153]

[1] Dilatometer data.

3.4. Pressure-Induced Phase Transitions in the $A_2M_3O_{12}$ Family

Many NTE compounds in the $A_2M_3O_{12}$ family are also sensitive to pressure due to their open framework structures. Materials that adopt the orthorhombic structure at room temperature tend to undergo a structural change to the denser monoclinic structure at very low pressures [155–157], which is akin to the temperature-induced phase transition mentioned above. In addition, irreversible amorphization is observed in many of these compounds at higher pressures ranging from 5 to 20 GPa [67,155,157–161]. This is not surprising, as the flexible, low-density frameworks of the $A_2M_3O_{12}$ family can readily distort or transform to denser crystalline polymorphs. Non-hydrostatic conditions favor this behavior, and can shift the onset of amorphization to even lower pressures. For a number of compositions, distinct new phases were formed at intermediate pressures. To date, it is impossible to predict the pressure and nature of these intriguing phase transitions for unstudied compositions, thus the high pressure behavior in this family still warrants further experimental and theoretical investigation. A small number of representative materials will be discussed in the following sections. For a more comprehensive summary of the high pressure behavior of these materials, the reader is referred to a review recently published by Young et al. [162].

3.4.1. High Pressure Behavior of NTE Tungstates

Orthorhombic $Sc_2W_3O_{12}$ is thermodynamically stable in a wide temperature range from −263 to at least 800 °C. However, even moderate pressure destabilizes this phase. Garg et al. studied the pressure-induced structural changes of $Sc_2W_3O_{12}$ using Raman scattering and X-ray diffraction [160]. Their work showed that $Sc_2W_3O_{12}$ transformed to a monoclinic phase near 0.28 GPa and converted to another denser monoclinic phase at 1.6 GPa. Both transitions were reversible upon decompression. Above 6.5 GPa, $Sc_2W_3O_{12}$ became increasingly disordered and irreversibly evolved into an amorphous state. Changes in the frequencies of the bending and asymmetric modes in the Raman spectra revealed that the polyhedra in the structure were highly distorted at this stage. Secco's impedance spectroscopy study indicated that the conductivity of $Sc_2W_3O_{12}$ increased with increasing pressure, making it a potential candidate for applications in pressure-sensing [163,164].

Orthorhombic $Al_2W_3O_{12}$ exhibited similar pressure-induced phase transition behavior. The orthorhombic phase converted to two distinct monoclinic structures at 0.5 GPa and 3.4 GPa, respectively, both of which were assigned to the space group $P2_1$ [165]. At 18 GPa, amorphization was observed. The higher phase transition pressures can be attributed to the smaller size of Al^{3+} and the resulting stiffer octahedra. In contrast to $Sc_2W_3O_{12}$ and $Al_2W_3O_{12}$, orthorhombic $Zr_2WP_2O_{12}$ remained stable up to ~1.7 GPa, and showed a gradual phase transition to a monoclinic cell (space group $P2_1/n$) above this pressure. In contrast to the other tungstates, no doubling of the number of formula units per unit cell and thus the cell volume was necessary to account for all peaks [161]. A second monoclinic phase was observed above 3.7 GPa (space group $P2_1/n$), followed by formation of a triclinic phase above 7.4 GPa (space group P1 or P-1) and irreversible amorphization above 14 GPa. Monoclinic $In_2W_3O_{12}$ also underwent a phase change in the pressure range of 1.9 to 2.7 GPa, but the lattice constants of the high-pressure cell could not be determined due to the coexistence of the two phases [158]. Unlike the above compounds, orthorhombic $Y_2W_3O_{12}$ transformed directly to a disordered phase at 3 GPa without intermediate crystalline high-pressure polymorphs [166].

3.4.2. High Pressure Behavior of NTE Molybdates

Several molybdates show comparable behavior to their tungstate counter parts. Varga et al. found that $Sc_2Mo_3O_{12}$ undergoes similar phase transitions as $Sc_2W_3O_{12}$ at comparable pressures [155]. A phase transition to monoclinic symmetry (space group $P2_1/a$) was observed at 0.25 GPa followed by conversion to a different monoclinic cell between 2.5 and 3.0 GPa. Above 8 GPa, broadening of diffraction peaks indicated successive amorphization. Monoclinic $Al_2Mo_3O_{12}$, $Fe_2Mo_3O_{12}$ and $Ga_2Mo_3O_{12}$ undergo identical phase transition

sequences to two denser monoclinic phases at pressures between 2.5 (space group $P2_1/a$) and 6 GPa (unknown space group) [167]. Young et al. showed that orthorhombic $Y_2Mo_3O_{12}$ underwent a phase transition to the low temperature monoclinic phase (space group $P2_1/a$) below 0.13 GPa. Surprisingly, no other pressure induced crystalline-to-crystalline phase transitions or amorphization were detected up to 4.9 GPa. Similarly, no phase transitions were observed for monoclinic $Cr_2Mo_3O_{12}$ up to 8.9 GPa [162].

While predictions of CTEs in $A_2M_3O_{12}$ materials are possible based on the ionic radii of the A site cations, no correlations between the metals present in the structure and the pressure induced phase transition behavior of these materials have been found. The ability to predict where a novel material may undergo a pressure induced phase transition would be highly beneficial for implementation in industries such as microelectronics, thermo shock resistant materials and aerospace.

4. Controllable Thermal Expansion in the $A_2M_3O_{12}$ Family

The $A_2M_3O_{12}$ structure displays excellent tolerance towards elemental substitution of both the A-site and M-site, which holds the potential for tuning the overall thermal expansion of materials. Thermal expansion coefficients can be tailored by either formation of composites or chemical modification of single-phase materials. Sleight's group began to prepare solid solutions with two or three trivalent cations as early as 1997 [58]. A number of compounds with NTE properties were synthetized successfully, such as $ScAlW_3O_{12}$, $ScGaW_3O_{12}$, $ScInW_3O_{12}$ and $ScHoW_3O_{12}$. They also effectively modulated the thermal expansion coefficient of $Al_2W_3O_{12}$ by doping with different ratios of In^{3+}. Finally, after adding trace amounts of Sc^{3+}, the zero-expansion material $Al_{1.68}Sc_{0.02}In_{0.3}W_3O_{12}$ was successfully prepared, which was a significant achievement that stimulated further research. Near-zero thermal expansion materials are attractive when dimensionally stable materials are desired. Design of intrinsic zero expansion materials through solid solution formation and heterogenous composite formation are the two main approaches to controlling thermal expansion coefficients of materials in applications.

4.1. Heterogeneous Composites

Composites that contain positive and negative thermal expansion materials present a straightforward method for the fabrication of controllable thermal expansion materials. However, for ceramic composites, this method requires two materials that possess excellent thermal stability and no reactivity with each other at the temperatures used for sintering. The first reports used an excess of MoO_3 in the preparation of $Fe_{2-x}Sc_xMo_3O_{12}$ to form a $Fe_{0.4}Sc_{1.6}Mo_3O_{12}/MoO_3$ composite with CTEs as low as 0.2×10^{-6} °C^{-1} [168]. To further reduce expansion and based on stability considerations, Yanase et al. chose $ZrSiO_4$, which possesses good chemical stability and low thermal expansion, to fabricate $ZrSiO_4/Y_2W_3O_{12}$ composites [169]. XRD analysis showed that no reactions occurred during sintering. An average linear thermal expansion coefficient of -0.08×10^{-6} °C^{-1} was measured from 25 to 1000 °C. Metal matrix composites with aluminum have also been explored [170,171]. More recent work has focused on ceramic composites that contain $Zr_2MP_2O_{12}$ (M = Mo, W) compositions, which do not undergo temperature or pressure-induced phase transitions [172–174]. Results from these approaches are summarized in Table 5.

4.2. Solid Solution Formation

The expansion behavior of the composites described above depends on their microstructures and interaction between the phases. Possible shortcomings of composites include interfacial mismatch, thermal stress at interfaces and potential chemical reactions. In addition, reproducibility between specimens and repeated thermal cycles can be less than optimal. In principle, solid solution formation through ion substitution provides an effective way of controlling thermal expansion coefficients of single-phase materials while circumventing the potential shortcomings of composites.

Table 5. Ceramic zero thermal expansion composites containing $A_2M_3O_{12}$ materials.

Compositions	dL/L$_0$ ($\times 10^{-6}$ °C^{-1})	T Range (°C)	Ref.
$Fe_{0.4}Sc_{1.6}Mo_3O_{12}/MoO_3$	0.2	25–500	[168]
$ZrSiO_4/Y_2W_3O_{12}$	−0.08	25–1000	[169]
$Al/ZrMgMo_3O_{12}$	0.77	25–400	[170]
$Al/Zr_2WP_2O_{12}$	−0.0021	20–600	[171]
$Sc_2W_3O_{12}/(ZrO_2+Y_2O_3)$	1.04	25–500	[175]
$Zr_2WP_2O_{12}/ZrV_{0.6}P_{1.4}O_7$	−0.029	25–500	[172]
$Zr_2MoP_2O_{12}/ZrO_2$	−0.0065	25–700	[173]
$Zr_2WP_2O_{12}/ZrO_2$	−0.09	25–700	[174]

4.2.1. Single Ion Substitution at the A/M Site

The first systematic studies targeted at tuning the expansion and phase transition behavior in $A_2M_3O_{12}$ materials were carried out by Sugimoto et al. by dilatometry [115] and Ari et al. by diffraction based methods [100]. Dilatometry based results may suffer from specimen-to-specimen variability. Ari's research on molybdates with mixtures of Al/Cr, Al/Fe and Cr/Fe on the A-site elegantly demonstrated that both phase transition temperatures and expansion coefficients can be tuned. However, all of the compounds investigated in their work displayed transition temperatures of 200 °C or higher. Low expansion and decreased transition temperatures were achieved by doping with lanthanides, however, many of these materials still showed hygroscopic tendencies when phase transition temperatures below room temperature were achieved [91–93]. Dasgupta et al. [118] synthesized $Al_{2-x}Sc_xW_3O_{12}$, which can be regarded as a mixture between $Sc_2W_3O_{12}$ with NTE and $Al_2W_3O_{12}$ with PTE. The value of x was varied from 0 to 2.0 to identify the optimum composition to achieve the least expansion. All compositions formed a single orthorhombic phase. For x = 1.5, the lowest coefficient of thermal expansion was observed, which was -0.15×10^{-6} °C^{-1} from 25 to 700 °C. $Al_{0.5}Sc_{1.5}W_3O_{12}$ also exhibited high in-line transmittance in the mid infrared wavelength range, making it a candidate for application in IR night vision devices. Other near-zero thermal expansion compounds prepared by single ion substitution are listed in Table 6.

Table 6. Near-zero thermal expansion compounds prepared by single ion substitution. CTEs are based on diffraction data unless otherwise indicated.

Compound	α_l ($\times 10^{-6}$ °C^{-1})	T Range (°C)	Ref.
$Al_{0.3}Sc_{1.7}Mo_3O_{12}$	−0.73	25–450	[111]
$Al_2Mo_{0.5}W_{2.5}O_{12}$	0.05 [1]	25–800	[106]
$Al_{0.5}Sc_{1.5}W_3O_{12}$	−0.32	25–600	[118]
$Fe_{0.4}Sc_{1.6}Mo_3O_{12}$	−0.83	25–800	[113]
$Fe_{0.7}Sc_{1.3}Mo_3O_{12}$	0.09	250–800	[113]
$ErFeMo_3O_{12}$	−0.60	180–400	[90]
$FeLuMo_3O_{12}$	0.99	200–800	[91]
$In_{1.3}Cr_{0.7}Mo_3O_{12}$	−0.76	400–750	[176]
$InCrMo_3O_{12}$	0.94	400–750	[176]
$Sc_{1.5}Cr_{0.5}Mo_3O_{12}$	−0.51	25–800	[109]
$Sc_{1.3}Cr_{0.7}Mo_3O_{12}$	−0.47	25–800	[109]
$Y_{0.25}Ce_{1.75}W_3O_{12}$	−0.82 [1]	182–700	[97]
$Yb_{0.6}Fe_{1.4}Mo_3O_{12}$	0.55	300–500	[177]

[1] Dilatometer data.

4.2.2. Aliovalent Ion Substitution at the A/M Site

Several aliovalently substituted materials display close to zero expansion. The first examples were $MgZrMo_3O_{12}$ and $MgHfMo_3O_{12}$, for which intrinsic α_l values of 0.13×10^{-6} and 1.02×10^{-6} °C^{-1} have been reported [126,138]. Partial substitution by tungsten can further lower the intrinsic CTE of $MgHfMo_{2.5}W_{0.5}O_{12}$ to -0.08×10^{-6} °C^{-1} [129]. Several compositions in which In^{3+} or Cr^{3+} were introduced on the A-site also display very

low intrinsic expansion [123,147,178]. Recently, $ZrFeMo_2VO_{12}$, a new near-zero thermal expansion material, was prepared using solid state methods by D. Chen et al. [81] to adjust the thermal expansion of $Fe_2Mo_3O_{12}$. The mechanism of CTE reduction was explained by the lower average expansion of the Zr(Fe)-*O*-V(Mo) bonds compared to Fe-*O*-Mo bonds, because Zr-O and V-O bonds are stiffer than Fe-O bonds. At the same time, double ion substitution also reduced the phase transition temperature of $Fe_2Mo_3O_{12}$ due to the smaller electronegativity of Zr^{4+}/V^{5+} compared to Fe^{3+}/Mo^{6+}. Additional results using aliovalent ion substitution are listed in Table 7.

Table 7. Near-zero thermal expansion compounds prepared by aliovalent ion substitution. CTEs are based on diffraction data.

Compound	α_l ($\times 10^{-6}$ °C^{-1})	T Range (°C)	Ref.
$MgZrMo_3O_{12}$	0.13	25–450	[138]
$MgHfMo_3O_{12}$	1.02	25–740	[126]
$HfMgMo_{2.5}W_{0.5}O_{12}$	−0.08	25–400	[129]
$Cr_{0.3}(MgZr)_{0.85}Mo_3O_{12}$	0.62	127–727	[123]
$In_{0.5}(MgZr)_{0.75}Mo_3O_{12}$	−0.16	100–500	[144]
$In(MgHf)_{0.5}Mo_3O_{12}$	−0.40	225–650	[147]
$ZrFeMo_2VO_{12}$	0.68	150–300	[130]
$(MgHf)_{0.83}ScW_{2.25}P_{0.83}O_{12-\delta}$	−1.03	−18–300	[150]
$Cr_{0.5}ScZr_{0.5}Mo_{2.5}V_{0.5}O_{12}$	0.95	−192–300	[153]
$Cr_{0.8}Sc_{0.7}Zr_{0.5}M_{o2.5}V_{0.5}O_{12}$	0.84	−94–300	[153]
$Sc_{1.5}Zr_{0.5}Mo_{2.5}V_{0.5}O_{12}$	−0.07	−192–300	[153]

5. Potential Challenges for Use of NTE Materials

In addition to moisture absorption and phase transitions, some additional factors need to be improved for NTE materials in the $A_2M_3O_{12}$ family to achieve their full potential. For example, many composites have low mechanical strength, which limits their applications. Several attempts to address this issue have been reported. Liu et al. prepared $Al/Y_2Mo_3O_{12}$ composites through uniaxial compression, which improved mechanical strength and conductivity [179]. Yang et al. [72] used a vacuum hot-pressing method to synthetize $ZrMgMo_3O_{12}/Al$ composites, which possessed both high strength and low thermal expansion [180].

6. Conclusions

The applications of $A_2M_3O_{12}$ materials as functional materials are limited, as additional desirable properties apart from low CTEs are necessary. Further exploration of their ionic conductivity could prove useful [181–183]. The ability of many ions in the structure to participate in redox reactions may have potential applications in sensing or batteries [184–191]. Researchers have started to enrich the physical or chemical properties of NTE materials with some success, which may lead to additional applications for these materials. For example, $ZrScMo_2VO_{12}$ and $HfScW_2PO_{12}$ show interesting photoluminescence properties [132,133], making them potential temperature-stable photoelectric materials for use in the field of light emitting diodes (LED). The material $(HfSc)_{0.83}W_{2.25}P_{0.83}O_{12-\delta}$ also displays photoluminescence, and may also show oxygen ion conductivity due to its composition [150]. NTE materials have been widely studied because of their abnormal thermal expansion properties and their potential for developing near-zero thermal expansion materials. These functional materials can effectively improve adverse effects on structure and precision of many devices. Compared to other NTE families, the $A_2M_3O_{12}$ family has excellent tunability through ion substitution and a wide NTE range. Despite challenges arising from hygroscopicity and phase transitions, the $A_2M_3O_{12}$ family still attracts much attention from researchers and warrants further exploration. Future directions for studies may include efforts dedicated to (1) in-depth research on CTEs and phase transitions of novel materials; (2) elucidation of the mechanism of pressure induced phase transitions; (3) searches for non-hygroscopic compositions with strong NTE performance;

(4) extending the NTE temperature range to lower temperatures; and (5) investigating and enhancing value-added properties like electrical conductivity, thermal conductivity, mechanical properties and photonic properties.

Funding: The authors would like to thank National Natural Science Foundation of China (No.51602280 and No.51102207), Qing Lan Project of Jiangsu Province, Postgraduate Research & Practice Innovation Program of Jiangsu Province (SJCX18-0794).

Conflicts of Interest: The authors declare no conflict of interest.

References

1. Chapman, K.W.; Chupas, P.J.; Kepert, C.J. Direct observation of a transverse vibrational mechanism for negative thermal expansion in $Zn(CN)_2$: An atomic pair distribution function analysis. *J. Am Chem. Soc.* **2005**, *127*, 15630–15636. [CrossRef]
2. Chapman, K.W.; Chupas, P.J.; Kepert, C.J. Compositional dependence of negative thermal expansion in the Prussian blue analogues (MPt^{IV})-$Pt^{II}(CN)_6$ (M = Mn, Fe, Co, Ni, Cu, Zn, Cd). *J. Am Chem. Soc.* **2006**, *128*, 7009–7014. [CrossRef] [PubMed]
3. Goodwin, A.L.; Kepert, C.J. Negative thermal expansion and low-frequency modes in cyanide-bridged framework materials. *Phys. Rev. B* **2005**, *71*, 140301(R). [CrossRef]
4. Margadonna, S.; Prassides, K.; Fitch, A.N. Zero thermal expansion in a Prussian blue analogue. *J. Am. Chem. Soc.* **2004**, *126*, 15390–15391. [CrossRef]
5. Matsuda, T.; Kim, J.E.; Ohoyama, K.; Moritomo, Y. Universal thermal response of the Prussian blue lattice. *Phys. Rev. B* **2009**, *79*. [CrossRef]
6. Adak, S.; Daemen, L.L.; Hartl, M.; Williams, D.; Summerhill, J.; Nakotte, H. Thermal expansion in 3d-metal Prussian Blue Analogs-A survey study. *J. Solid State Chem.* **2011**, *184*, 2854–2861. [CrossRef]
7. Greve, B.K.; Martin, K.L.; Lee, P.L.; Chupas, P.J.; Chapman, K.W.; Wilkinson, A.P. Pronounced Negative Thermal Expansion from a Simple Structure: Cubic ScF_3. *J. Am. Chem. Soc.* **2010**, *132*, 15496–15498. [CrossRef]
8. Hester, B.R.; Hancock, J.C.; Lapidus, S.H.; Wilkinson, A.P. Composition, Response to Pressure, and Negative Thermal Expansion in $M^{II}B^{IV}F_6$ (M = Ca, Mg; B = Zr, Nb). *Chem. Mater.* **2017**, *29*, 823–831. [CrossRef]
9. Li, C.W.; Tang, X.; Munoz, J.A.; Keith, J.B.; Tracy, S.J.; Abernathy, D.L.; Fultz, B. Structural Relationship between Negative Thermal Expansion and Quartic Anharmonicity of Cubic ScF_3. *Phys. Rev. Lett.* **2011**, *107*. [CrossRef]
10. Ticknor, J.O.; Hester, B.R.; Adkins, J.W.; Xu, W.Q.; Yakovenko, A.A.; Wilkinson, A.P. Zero Thermal Expansion and Abrupt Amorphization on Compression in Anion Excess ReO_3-Type Cubic $YbZrF_7$. *Chem. Mater.* **2018**, *30*, 3071–3077. [CrossRef]
11. Baxter, S.J.; Hester, B.R.; Wright, B.R.; Wilkinson, A.P. Controlling the Negative Thermal Expansion and Response to Pressure in ReO_3-type Fluorides by the Deliberate Introduction of Excess Fluoride: $Mg_{1-x}Zr_{1+x}F_{6+2x}$, x = 0.15, 0.30, 0.40, and 0.50. *Chem. Mater.* **2019**, *31*, 3440–3448. [CrossRef]
12. Chatterji, T.; Zbiri, M.; Hansen, T.C. Negative thermal expansion in ZnF_2. *Appl. Phys. Lett.* **2011**, *98*. [CrossRef]
13. Han, F.; Hu, L.; Liu, Z.N.; Li, Q.; Wang, T.; Ren, Y.; Deng, J.X.; Chen, J.; Xing, X.R. Local structure and controllable thermal expansion in the solid solution $(Mn_{1-x}Ni_x)ZrF_6$. *Inorg. CHem. Front.* **2017**, *4*, 343–347. [CrossRef]
14. Hancock, J.C.; Chapman, K.W.; Halder, G.J.; Morelock, C.R.; Karlan, B.S.; Gallington, L.C.; Bongiorno, A.; Han, C.; Zhou, S.; Wilkinson, A.P. Large Negative Thermal Expansion and Anomalous Behavior on Compression in Cubic ReO_3-Type $A^{II}B^{IV}F_6$: $CaZrF_6$ and $CaHfF_6$. *Chem. Mater.* **2015**, *27*, 3912–3918. [CrossRef]
15. Morelock, C.R.; Gallington, L.C.; Wilkinson, A.P. Evolution of Negative Thermal Expansion and Phase Transitions in $Sc_{1-x}Ti_xF_3$. *Chem. Mater.* **2014**, *26*, 1936–1940. [CrossRef]
16. Yang, C.; Zhang, Y.G.; Bai, J.M.; Qu, B.Y.; Tong, P.; Wang, M.; Lin, J.C.; Zhang, R.R.; Tong, H.Y.; Wu, Y.; et al. Crossover of thermal expansion from positive to negative by removing the excess fluorines in cubic ReO_3-type $TiZrF_{7-x}$. *J. Mater. Chem. C* **2018**, *6*, 5148–5152. [CrossRef]
17. Takenaka, K.; Takagi, H. Giant negative thermal expansion in Ge-doped anti-perovskite manganese nitrides. *Appl. Phys. Lett.* **2005**, *87*. [CrossRef]
18. Sun, Y.; Wang, C.; Wen, Y.C.; Chu, L.H.; Pan, H.; Niez, M. Negative Thermal Expansion and Magnetic Transition in Anti-Perovskite Structured $Mn_3Zn_{1-x}Sn_xN$ Compounds. *J. Am. Ceram. Soc.* **2010**, *93*, 2178–2181. [CrossRef]
19. Hamada, T.; Takenaka, K. Giant negative thermal expansion in antiperovskite manganese nitrides. *J. Appl. Phys.* **2011**, *109*. [CrossRef]
20. Takenaka, K.; Ichigo, M.; Hamada, T.; Ozawa, A.; Shibayama, T.; Inagaki, T.; Asano, K. Magnetovolume effects in manganese nitrides with antiperovskite structure. *Sci. Technol. Adv. Mater.* **2014**, *15*, 015009. [CrossRef]
21. Iikubo, S.; Kodama, K.; Takenaka, K.; Takagi, H.; Shamoto, S. Magnetovolume effect in $Mn_3Cu_{1-x}Ge_xN$ related to the magnetic structure: Neutron powder diffraction measurements. *Phys. Rev. B* **2008**, *77*. [CrossRef]
22. Huang, R.J.; Li, L.F.; Cai, F.S.; Xu, X.D.; Qian, L.H. Low-temperature negative thermal expansion of the antiperovskite manganese nitride Mn_3CuN codoped with Ge and Si. *Appl. Phys. Lett.* **2008**, *93*. [CrossRef]
23. Iikubo, S.; Kodama, K.; Takenaka, K.; Takagi, H.; Takigawa, M.; Shamoto, S. Local Lattice Distortion in the Giant Negative Thermal Expansion Material $Mn_3Cu_{1-x}Ge_xN$. *Phys. Rev. Lett.* **2008**, *101*. [CrossRef] [PubMed]

24. Huang, R.J.; Liu, Y.Y.; Fan, W.; Tan, J.; Xiao, F.R.; Qian, L.H.; Li, L.F. Giant Negative Thermal Expansion in $NaZn_{13}$-Type La(Fe, Si, Co)$_{13}$ Compounds. *J. Am Chem. Soc.* **2013**, *135*, 11469–11472. [CrossRef] [PubMed]
25. Li, S.P.; Huang, R.J.; Zhao, Y.Q.; Li, W.; Wang, W.; Huang, C.J.; Gong, P.F.; Lin, Z.S.; Li, L.F. Broad Negative Thermal Expansion Operation-Temperature Window Achieved by Adjusting Fe-Fe Magnetic Exchange Coupling in La(Fe,Si)$_{13}$ Compounds. *Inorg. Chem.* **2015**, *54*, 7868–7872. [CrossRef]
26. Li, S.P.; Huang, R.J.; Zhao, Y.Q.; Wang, W.; Han, Y.M.; Li, L.F. Zero Thermal Expansion Achieved by an Electrolytic Hydriding Method in La(Fe, Si)$_{13}$ Compounds. *Adv. Funct. Mater.* **2017**, *27*. [CrossRef]
27. Song, Y.Z.; Huang, R.J.; Liu, Y.; Zhang, Z.H.; Huang, Q.Z.; Jiang, Y.; Wang, S.G.; Li, L.F.; Xing, X.R.; Chen, J. Magnetic-Field-Induced Strong Negative Thermal Expansion in La(Fe,Al)$_{13}$. *Chem. Mater.* **2020**, *32*, 7535–7541. [CrossRef]
28. Sun, W.T.; Zhang, H.; Li, W.; Huang, R.J.; Zhao, Y.Q.; Wang, W.; Li, L.F. Controllable negative thermal expansion in $NaZn_{13}$-type La(Fe, Co, Al)$_{13}$ compounds. *AIP Adv.* **2020**, *10*. [CrossRef]
29. Hu, J.Y.; Lin, K.; Cao, Y.L.; Yu, C.Y.; Li, W.J.; Huang, R.J.; Fischer, H.E.; Kato, K.; Song, Y.Z.; Chen, J.; et al. Adjustable Magnetic Phase Transition Inducing Unusual Zero Thermal Expansion in Cubic RCo_2-Based Intermetallic Compounds (R = Rare Earth). *Inorg. Chem.* **2019**, *58*, 5401–5405. [CrossRef] [PubMed]
30. Salvador, J.R.; Gu, F.; Hogan, T.; Kanatzidis, M.G. Zero thermal expansion in YbGaGe due to an electronic valence transition. *Nature* **2003**, *425*, 702–705. [CrossRef] [PubMed]
31. Gruner, M.E.; Keune, W.; Roldan Cuenya, B.; Weis, C.; Landers, J.; Makarov, S.I.; Klar, D.; Hu, M.Y.; Alp, E.E.; Zhao, J.; et al. Element-Resolved Thermodynamics of Magnetocaloric $LaFe_{13-x}Si_x$. *Phys. Rev. Lett.* **2015**, *114*. [CrossRef]
32. Evans, J.S.O.; Hu, Z.; Jorgensen, J.D.; Argyriou, D.N.; Short, S.; Sleight, A.W. Compressibility, Phase Transitions, and Oxygen Migration in Zirconium Tungstate, ZrW_2O_8. *Science* **1997**, *275*, 61–65. [CrossRef] [PubMed]
33. Evans, J.S.O.; Mary, T.A.; Vogt, T.; Subramanian, M.A.; Sleight, A.W. Negative Thermal Expansion in ZrW_2O_8 and HfW_2O_8. *Chem. Mater.* **1996**, *8*, 2809–2823. [CrossRef]
34. Mary, T.A.; Evans, J.S.O.; Vogt, T.; Sleight, A.W. Negative Thermal Expansion from 0.3 to 1050 Kelvin in ZrW_2O_8. *Science* **1996**, *272*, 90–92. [CrossRef]
35. Lind, C.; Wilkinson, A.P.; Hu, Z.B.; Short, S.; Jorgensen, J.D. Synthesis and Properties of the Negative Thermal Expansion Material Cubic $ZrMo_2O_8$. *Chem. Mater.* **1998**, *10*, 2335–2337. [CrossRef]
36. Perottoni, C.A.; da Jornada, J.A.H. Pressure-induced amorphization and negative thermal expansion in ZrW_2O_8. *Science* **1998**, *280*, 886–889. [CrossRef] [PubMed]
37. Pryde, A.K.A.; Hammonds, K.D.; Dove, M.T.; Heine, V.; Gale, J.D.; Warren, M.C. Rigid Unit Modes and the Negative Thermal Expansion in ZrW_2O_8. *Phase Transit.* **1997**, *61*, 141–153. [CrossRef]
38. Ramirez, A.P.; Kowach, G.R. Large Low Temperature Specific Heat in the Negative Thermal Expansion Compound ZrW_2O_8. *Phys. Rev. Lett.* **1998**, *80*, 4903–4906. [CrossRef]
39. Korthuis, V.; Khosrovani, N.; Sleight, A.W.; Roberts, N.; Dupree, R.; Warren, W.W. Negative thermal expansion and phase transitions in the $ZrV_{2-x}P_xO_7$ series. *Chem. Mater.* **1995**, *7*, 412–417. [CrossRef]
40. Khosrovani, K.; Sleight, A.W.; Vogt, T. Structure of ZrV_2O_7 from −263 to 470 °C. *J. Solid State Chem.* **1997**, *132*, 355–360. [CrossRef]
41. Carlson, S.; Andersen, A.M.K. High-pressure properties of TiP_2O_7, ZrP_2O_7 and ZrV_2O_7. *J. Appl. Crystallogr.* **2001**, *34*, 7–12. [CrossRef]
42. Xing, X.R.; Zhu, Z.Q.; Qiu, X.P.; Liu, G.R. Zero-thermal expansion and heat capacity of zirconium pyrovanadate doped with zirconia and vanadium (V) oxide. *Rare Metals* **2001**, *20*, 1–4.
43. Beccara, S.A.; Dalba, G.; Fornasini, P.; Grisenti, R.; Sanson, A. Local thermal expansion in a cuprite structure: The case of Ag_2O. *Phys. Rev. Lett.* **2002**, *89*, 025503. [CrossRef] [PubMed]
44. Tiano, W.; Dapiaggi, M.; Artioli, G. Thermal expansion in cuprite-type structures from 10 K to decomposition temperature: Cu_2O and Ag_2O. *J. Appl. Crystallogr.* **2003**, *36*, 1461–1463. [CrossRef]
45. Kennedy, B.J.; Kubota, Y.; Kato, K. Negative thermal expansion and phase transition behaviour in Ag_2O. *Solid State Commun.* **2005**, *136*, 177–180. [CrossRef]
46. Fornasini, P.; Dalba, G.; Grisenti, R.; Purans, J.; Vaccari, M.; Rocca, F.; Sanson, A. Local behaviour of negative thermal expansion materials. *Nucl. Inst. Methods Phys. Res. B* **2006**, *246*, 180–183. [CrossRef]
47. Sanson, A.; Rocca, F.; Dalba, G.; Fornasini, P.; Grisenti, R.; Dapiaggi, M.; Artioli, G. Negative thermal expansion and local dynamics in Cu_2O and Ag_2O. *Phys. Rev. B* **2006**, *73*. [CrossRef]
48. Evans, J.S.O.; Mary, T.A.; Sleight, A.W. Negative Thermal Expansion Materials. *Phys. B* **1998**, *241–243*, 311–316. [CrossRef]
49. Forster, P.M.; Sleight, A.W. Negative Thermal Expansion in $Y_2W_3O_{12}$. *Int. J. Inorg. Mater.* **1999**, *1*, 123–127. [CrossRef]
50. Mary, T.A.; Sleight, A.W. Bulk thermal expansion for tungstate and molybdates of the type $A_2M_3O_{12}$. *J. Mater. Res.* **1999**, *14*, 912–915. [CrossRef]
51. Nassau, K.; Levinstein, H.J.; Loiacono, G.M. A comprehensive study of trivalent tungstates and molybdates of the type $L_2(MO_4)_3$. *Phys. Chem. Solids* **1965**, *26*, 1815–1816. [CrossRef]
52. Cao, W.G.; Li, Q.; Lin, K.; Liu, Z.N.; Deng, J.X.; Chen, J.; Xing, X.R. Phase transition and negative thermal expansion in orthorhombic $Dy_2W_3O_{12}$. *RSC Adv.* **2016**, *6*, 96275–96280. [CrossRef]
53. Roy, M.; Choudhary, R.N.P.; Acharya, H.N. X-ray and thermal studies of ferroelectric $Dy_2(MoO_4)_3$. *J. Therm. Anal.* **1989**, *35*, 1471–1476. [CrossRef]

54. Jeitschko, W. Comprehensive X-ray study of the ferroelectric-ferroelastic and paraelectric-paraelastic phases of gadolinium molybdate. *Acta Crystallogr. B* **1972**, *28*, 60–76. [CrossRef]
55. Evans, J.S.O.; Mary, T.A.; Sleight, A.W. Negative thermal expansion in $Sc_2(WO_4)_3$. *J. Solid State Chem.* **1998**, *137*, 148–160. [CrossRef]
56. Liu, H.F.; Yang, L.; Zhang, Z.P.; Pan, K.M.; Zhang, F.; Cheng, H.H.; Zeng, X.H.; Chen, X.B. Preparation and optical, nanomechanical, negative thermal expansion properties of $Sc_2W_3O_{12}$ thin film grown by pulsed laser deposition. *Ceram. Int.* **2016**, *42*, 8809–8814. [CrossRef]
57. Forster, P.M.; Yokochi, A.; Sleight, A.W. Enhanced Negative Thermal Expansion in $Lu_2W_3O_{12}$. *J. Solid State Chem.* **1998**, *140*, 157–158. [CrossRef]
58. Evans, J.S.O.; Mary, T.A.; Sleight, A.W. Negative Thermal Expansion in a Large Molybdate and Tungstate Family. *J. Solid State Chem.* **1997**, *133*, 580–583. [CrossRef]
59. Evans, J.S.O.; Mary, T.A. Structural phase transitions and negative thermal expansion in $Sc_2(MoO_4)_3$. *Int. J. Inorg. Mater.* **2000**, *2*, 143–151. [CrossRef]
60. Pernicone, N.; Fagherazzi, G. A new iron tungstate: $Fe_2W_3O_{12}$. *J. Inorg. Nucl. Chem.* **1969**, *31*, 3323–3324. [CrossRef]
61. Zhang, H.J.; Zhang, Q.; Du, H.L.; Jia, Q.L. Preparation and thermal expansion of $Fe_{2-x}Y_xW_3O_{12}$ powder by citrate sol-gel process. *Chem. Eng. Commun.* **2008**, *195*, 243–255. [CrossRef]
62. Harrison, W.T.A.; Chowdhry, U.; Machiels, C.J.; Sleight, A.W.; Cheetham, A.K. Preparation of ferric tungstate and its catalytic behavior toward methanol. *J. Solid State Chem.* **1985**, *60*, 101–106. [CrossRef]
63. Kendrick, E.; Swiatek, A.; Barker, J. Synthesis and characterisation of iron tungstate anode materials. *J. Power Sources* **2009**, *189*, 611–615. [CrossRef]
64. Sriraman, A.K.; Tyagi, A.K. A new method of $Fe_2(WO_4)_3$ preparation and its thermal stability. *Thermochim. Acta* **2003**, *406*, 29–33. [CrossRef]
65. Yang, Y.-M.; Li, L.-C.; Feng, M. Negative thermal expansion property of $Cr_2(WO_4)_3$ and $Cr_2(MoO_4)_3$. *Chin. J. Inorg. Chem.* **2007**, *23*, 382–386.
66. Yang, G.; Liu, X.S.; Sun, X.W.; Liang, E.J.; Zhang, W.F. Synthesis process control of low-thermal-expansion $Fe_2W_3O_{12}$ by suppressing the intermediate phase Fe_2WO_6. *Ceram. Int.* **2018**, *44*, 22032–22035. [CrossRef]
67. Gates, S.D.; Colin, J.A.; Lind, C. Non-hydrolytic sol-gel synthesis, properties, and high-pressure behavior of gallium molybdate. *J. Mater. Chem.* **2006**, *16*, 4214–4219. [CrossRef]
68. Sumithra, S.; Umarji, A.M. Negative thermal expansion in rare earth molybdates. *Solid State Sci.* **2006**, *8*, 1453–1458. [CrossRef]
69. Woodcock, D.A.; Lightfoot, P.; Ritter, C. Negative thermal expansion in $Y_2(WO_4)_3$. *J. Solid State Chem.* **2000**, *149*, 92–98. [CrossRef]
70. Zhang, Z.P.; Yang, L.; Liu, H.F.; Pan, K.M.; Wang, W.; Zeng, X.H.; Chen, X.B. Preparation and negative thermal expansion properties of $Y_2W_3O_{12}$ thin films grown by pulsed laser deposition. *Ceram. Int.* **2016**, *42*, 18902–18906. [CrossRef]
71. Xiao, X.L.; Cheng, Y.Z.; Peng, J.; Wu, M.M.; Chen, D.F.; Hu, Z.B.; Kiyanagi, R.; Fieramosca, J.S.; Short, S.; Jorgensen, J. Thermal expansion properties of $A_2(MO_4)_3$ (A = Ho and Tm; M = W and Mo). *Solid State Sci.* **2008**, *10*, 321–325. [CrossRef]
72. Sumithra, S.; Tyagi, A.K.; Umarji, A.M. Negative thermal expansion in $Er_2W_3O_{12}$ and $Yb_2W_3O_{12}$ by high temperature X-ray diffraction. *Mater. Sci. Eng. B* **2005**, *116*, 14–18. [CrossRef]
73. Dove, M.T.; Fang, H. Negative thermal expansion and associated anomalous physical properties: Review of the lattice dynamics theoretical foundation. *Rep. Prog. Phys.* **2016**, *79*, 066503. [CrossRef] [PubMed]
74. Mittal, R.; Gupta, M.K.; Chaplot, S.L. Phonons and anomalous thermal expansion behaviour in crystalline solids. *Prog. Mater. Sci.* **2018**, *92*, 360–445. [CrossRef]
75. Barrera, G.D.; Bruno, J.A.O.; Barron, T.H.K.; Allan, N.L. Negative thermal expansion. *J. Phys. Condens. Matter* **2005**, *17*, R217–R252. [CrossRef]
76. Dove, M.T.; Trachenko, K.O.; Tucker, M.G.; Keen, D.A. Rigid unit modes in framework structures: Theory, experiment and applications. *Transf. Processes Miner.* **2000**, *39*, 1–33.
77. Pryde, A.K.A.; Hammonds, K.D.; Dove, M.T.; Heine, V.; Gale, J.D.; Warren, M.C. Origin of the Negative Thermal Expansion in ZrW_2O_8 and ZrV_2O_7. *J. Phys. Condens. Matter* **1996**, *8*, 10973–10982. [CrossRef]
78. Tao, J.Z.; Sleight, A.W. The role of rigid unit modes in negative thermal expansion. *J. Solid State Chem.* **2003**, *173*, 442–448. [CrossRef]
79. Ernst, G.; Broholm, C.; Kowach, G.R.; Ramirez, A.P. Phonon density of states and negative thermal expansion in ZrW_2O_8. *Nature* **1998**, *396*, 147–149. [CrossRef]
80. Rimmer, L.H.N.; Dove, M.T. Simulation study of negative thermal expansion in yttrium tungstate $Y_2W_3O_{12}$. *J. Phys. Condens. Matter* **2015**, *27*, 185401. [CrossRef]
81. Romao, C.P.; Donegan, S.P.; Zwanziger, J.W.; White, M.A. Relationships between elastic anisotropy and thermal expansion in $A_2Mo_3O_{12}$ materials. *Chem. Phys. Phys. Chem.* **2016**, *18*, 30652–30661. [CrossRef]
82. Marinkovic, B.A.; Jardim, P.M.; de Avillez, R.R.; Rizzo, F. Negative thermal expansion in $Y_2Mo_3O_{12}$. *Solid State Sci.* **2005**, *7*, 1377–1383. [CrossRef]
83. Cao, W.G.; Zhu, H.; Liu, Z.N.; Deng, J.X.; Chen, J.; Xing, X.R. Phase transition and thermal expansion of $Ho_2W_3O_{12}$. *Inorg. Chem. Front.* **2016**, *73*, 111–114. [CrossRef]
84. Sumithra, S.; Umarji, A.M. Hygroscopicity and bulk thermal expansion $Y_2W_3O_{12}$. *Mater. Res. Bull.* **2005**, *40*, 167–176. [CrossRef]

85. Kol'tsova, T.N. X-ray Diffraction Study of $Y_2W_3O_{12} \bullet 3H_2O$. *Inorg. Mater.* **2001**, *37*, 1175–1177. [CrossRef]
86. Liang, E.; Huo, H.; Wang, J.; Chao, M. Effect of water species on the phonon modes in orthorhombic $Y_2(MoO_4)_3$ revealed by Raman spectroscopy. *J. Phys. Chem. C* **2008**, *112*, 6577–6581. [CrossRef]
87. Li, Z.Y.; Song, W.B.; Liang, E.J. Structures, Phase Transition, and Crystal Water of $Fe_{2-x}Y_xMo_3O_{12}$. *J. Phys. Chem. C* **2011**, *115*, 17806–17811. [CrossRef]
88. Li, Q.J.; Yuan, B.H.; Song, W.B.; Liang, E.J.; Yuan, B. The phase transition, hygroscopicity, and thermal expansion properties of $Yb_{2-x}Al_xMo_3O_{12}$. *Chin. Phys. B* **2012**, *21*, 046501. [CrossRef]
89. Liu, Q.Q.; Yu, Z.Q.; Che, G.F.; Yao, J.L.; Sun, X.J.; Cheng, X.N.; Yang, J. Synthesis and tunable thermal expansion properties of $Sc_{2-x}Y_xW_3O_{12}$ solid solutions. *Ceram. Int.* **2014**, *40*, 8195–8199. [CrossRef]
90. Cheng, Y.Z.; Wu, M.M.; Peng, J.; Xiao, X.L.; Li, Z.X.; Hu, Z.B.; Kiyanagi, R.; Fieramosca, J.S.; Short, S.; Jorgensen, J. Structures, thermal expansion properties and phase transitions of $Er_xFe_{2-x}(MoO_4)_3$ ($0.0 \leq x \leq 2.0$). *Solid State Sci.* **2007**, *9*, 693–698. [CrossRef]
91. Wu, M.M.; Peng, J.; Zu, Y.; Liu, R.D.; Hu, Z.B.; Liu, Y.T.; Chen, D.F. Thermal expansion properties of $Lu_{2-x}Fe_xMo_3O_{12}$. *Chin. Phys. B* **2012**, *21*, 116102. [CrossRef]
92. Wu, M.M.; Xiao, X.L.; Hu, Z.B.; Liu, Y.T.; Chen, D.F. Controllable thermal expansion and phase transition in $Yb_{2-x}Cr_xMo_3O_{12}$. *Solid State Sci.* **2009**, *11*, 325–329. [CrossRef]
93. Wu, M.M.; Hu, Z.B.; Liu, Y.T.; Chen, D.F. Thermal expansion properties of $Ln_{2-x}Cr_xMo_3O_{12}$ (Ln = Er and Y). *Mater. Res. Bull.* **2009**, *44*, 1943–1947. [CrossRef]
94. Liu, H.F.; Wang, X.C.; Zhang, Z.P.; Chen, X.B. Synthesis and thermal expansion properties of $Y_{2-x}La_xMo_3O_{12}$ (x = 0, 0.5, 2). *Ceram. Int.* **2012**, *38*, 6349–6352. [CrossRef]
95. Liu, H.F.; Zhang, W.; Zhang, Z.P.; Chen, X.B. Synthesis and negative thermal expansion properties of solid solutions $Yb_{2-x}La_xW_3O_{12}$ ($0 \leq x \leq 2$). *Ceram. Int.* **2012**, *38*, 2951–2956. [CrossRef]
96. Liu, H.F.; Zhang, Z.P.; Zhang, W.; Zeng, X.H.; Chen, X.B. Synthesis and negative thermal expansion property of $Y_{2-x}La_xW_3O_{12}$ ($0 \leq x \leq 2$). *Ceram. Int.* **2013**, *39*, 2781–2786. [CrossRef]
97. Liu, H.F.; Sun, W.K.; Zhang, Z.P.; Zhou, M.; Meng, X.D.; Zeng, X.H. Tailorable thermal expansion and hygroscopic properties of cerium-substituted $Y_2W_3O_{12}$ ceramics. *J. Alloys Compd.* **2018**, *751*, 49–55. [CrossRef]
98. Cheng, Y.G.; Liu, X.S.; Song, W.B.; Yuan, B.H.; Wang, X.L.; Chao, M.J.; Liang, E.J. Relationship between hygroscopicity reduction and morphology evolution of $Y_2Mo_3O_{12}$ doped with $(LiMg)^{3+}$. *Mater. Res. Bull.* **2015**, *65*, 273–278. [CrossRef]
99. Liu, X.S.; Yuan, B.H.; Cheng, Y.G.; Ge, X.H.; Liang, E.J.; Zhang, W.F. Avoiding the invasion of H_2O into $Y_2Mo_3O_{12}$ by coating with C_3N_4 to improve negative thermal expansion properties. *Phys. Chem. Chem. Phys.* **2017**, *19*, 13443–13448. [CrossRef]
100. Ari, M.; Jardim, P.M.; Marinkovic, B.A.; Rizzo, F.; Ferreira, F.F. Thermal expansion of $Cr_{2x}Fe_{2-2x}Mo_3O_{12}$, $Al_{2x}Fe_{2-2x}Mo_3O_{12}$ and $Al_{2x}Cr_{2-2x}Mo_3O_{12}$ solid solutions. *J. Solid State Chem.* **2008**, *181*, 1472–1479. [CrossRef]
101. Sleight, A.W.; Brixner, L.H. A New Ferroelastic Transition in Some $A_2(MO_4)_3$ Molybdates and Tungstates. *J. Solid State Chem.* **1973**, *7*, 172–174. [CrossRef]
102. Marinkovic, B.A.; Ari, M.; Jardim, P.M.; de Avillez, R.R.; Rizzo, F.; Ferreira, F.F. $In_2Mo_3O_{12}$: A low negative thermal expansion compound. *Thermochim. Acta* **2010**, *499*, 48–53. [CrossRef]
103. Liu, H.F.; Zhang, Z.P.; Ma, J.; Jun, Z.; Zeng, X.H. Effect of isovalent substitution on phase transition and negative thermal expansion of $In_{2-x}Sc_xW_3O_{12}$ ceramics. *Ceram. Int.* **2015**, *41*, 9873–9877. [CrossRef]
104. Tyagi, A.K.; Achary, S.N.; Mathews, M.D. Phase transition and negative thermal expansion in $A_2(MoO_4)_3$ system ($A=Fe^{3+}$, Cr^{3+} and Al^{3+}). *J. Alloys Compd.* **2002**, *339*, 207–210. [CrossRef]
105. Truitt, R.; Hermes, I.; Leright, A.; Sendecki, A.; Lind, C. Non-hydrolytic sol-gel synthesis of homogeneous $AlScMo_3O_{12}$. *Materials* **2015**, *8*, 700–716. [CrossRef]
106. Shen, R.; Wang, T.M. The synthesis and thermal expansion of $Al_2Mo_{3-x}W_xO_{12}$. *Rare Metal Mater. Eng.* **2004**, *33*, 91–95.
107. Liu, X.Z.; Hao, L.J.; Wu, M.M.; Ma, X.B.; Chen, D.F.; Liu, Y.T. The structure, thermal expansion and phase transition properties of $Ho_2Mo_{3-x}W_xO_{12}$ (x=0, 1.0, 2.0) solid solutions. *Mater. Res. Bull.* **2015**, *70*, 640–644. [CrossRef]
108. Zhang, Z.P.; Sun, W.K.; Zheng, Q.; Liu, H.F.; Zhou, M.; Wang, W.; Chen, X.B. Tuning the phase transition temperature of $Cr_2(MoO_4)_3$ by A-site substitution of scandium. *Ceram. Int.* **2018**, *44*, 22165–22171. [CrossRef]
109. Wu, M.M.; Peng, J.; Han, S.B.; Hu, Z.B.; Liu, Y.T.; Chen, D.F. Phase transition and negative thermal expansion properties of $Sc_{2-x}Cr_xMo_3O_{12}$. *Ceram. Int.* **2012**, *38*, 6525–6529. [CrossRef]
110. Gates, S.D. Cation Influence of Negative Thermal Expansion in the $A_2M_3O_{12}$ Family. Ph.D. Thesis, The University of Toledo, Toledo, OH, USA, 2008.
111. Wu, M.; Peng, J.; Cheng, Y.; Xiao, X.; Chen, D.; Hu, Z. Structural and controllable thermal expansion properties of $Sc_{2-x}Al_xMo_3O_{12}$. *J. Alloys Compd.* **2013**, *577*, 295–298. [CrossRef]
112. Sun, W.K.; Zhang, Z.P.; Liu, H.F.; Wang, W.; Zeng, X.H. Tailored phase transition temperature and negative thermal expansion of Sc-substituted $Fe_2Mo_3O_{12}$ synthesized by the co-precipitation method. *J. Alloys Compd.* **2019**, *794*, 1–7. [CrossRef]
113. Wu, M.M.; Liu, X.Z.; Chen, D.F.; Huang, Q.Z.; Wu, H.; Liu, Y.T. Structure, Phase Transition, and Controllable Thermal Expansion Behaviors of $Sc_{2-x}Fe_xMo_3O_{12}$. *Inorg. Chem.* **2014**, *53*, 9206–9212. [CrossRef]
114. Zhang, Z.P.; Wang, Y.N.; Sun, W.K.; Zhang, X.Y.; Liu, H.F.; Chen, X.B.; Zeng, X.H. Phase transition temperature and negative thermal expansion of Sc-substituted $In_2(MoO_4)_3$ ceramics. *J. Mater. Sci.* **2020**, *55*, 5730–5740. [CrossRef]

115. Sugimoto, T.; Aoki, Y.; Niwa, E.; Hashimoto, T.; Morito, Y. Thermal expansion and phase transition behavior of $Al_{2-x}M_x(WO_4)_3$ (M = Y, Ga and Sc) ceramics. *J. Ceram. Soc. Jpn.* **2007**, *115*, 176–181. [CrossRef]
116. Koseva, I.; Yordanova, A.; Tzvetkov, P.; Nikolov, V.; Nihtianova, D. Nanosized pure and Cr doped $Al_{2-x}In_x(WO_4)_3$ solid solutions. *Mater. Chem. Phys.* **2012**, *132*, 808–814. [CrossRef]
117. Zhang, F.; Lei, Y.; Zhang, Z.P.; Liu, H.F.; Zhang, X.Y.; Chen, X.B.; Zeng, X.H. Negative thermal expansion coefficient of Sc-doped indium tungstate ceramics synthesized by co-precipitation. *Ceram. Int.* **2020**, *46*, 7259–7267. [CrossRef]
118. Dasgupta, N.; Sorge, E.; Butler, B.; Wen, T.C.; Shetty, D.K.; Cambrea, L.R.; Harris, D.C. Synthesis and characterization of $Al_{2-x}Sc_x(WO_4)_3$ ceramics for low-expansion infrared-transmitting windows. *J. Mater. Sci.* **2012**, *47*, 6286–6296. [CrossRef]
119. Marinkovic, B.A.; Ari, M.; de Avillez, R.R.; Rizzo, F.; Ferreira, F.F.; Miller, K.J.; Johnson, M.B.; White, M.A. Correlation between AO_6 Polyhedral Distortion and Negative Thermal Expansion on Orthorhombic $Y_2Mo_3O_{12}$ and Related Materials. *Chem. Mater.* **2009**, *21*, 2886–2894. [CrossRef]
120. Li, S.L.; Ge, X.H.; Yuan, H.L.; Chen, D.X.; Guo, J.; Shen, R.F.; Chao, M.J.; Liang, E.J. Near-Zero Thermal Expansion and Phase Transitions in $HfMg_{1-x}Zn_xMo_3O_{12}$. *Front. Chem.* **2018**, *6*. [CrossRef] [PubMed]
121. Li, T.; Ge, X.H.; Liu, X.S.; Cheng, Y.G.; Liu, Y.M.; Yuan, H.L.; Li, S.L.; Liu, Y.Y.; Guo, J.; Sun, Q.; et al. Enhanced negative thermal expansion by solid solution of $HfMgMo_{1.5}W_{1.5}O_{12}$. *Mater. Express* **2016**, *6*, 515–520. [CrossRef]
122. Shen, R.F.; Yuan, B.H.; Li, S.L.; Ge, X.H.; Guo, J.; Liang, E.J. Near-zero thermal expansion of $Zr_xHf_{1-x}MgMo_3O_{12}$ in a larger temperature range. *Optik* **2018**, *165*, 1–6. [CrossRef]
123. Song, W.-B.; Wang, J.-Q.; Li, Z.-Y.; Liu, X.-S.; Yuan, B.-H.; Liang, E.-J. Phase transition and thermal expansion property of $Cr_{2-x}Zr_{0.5x}Mg_{0.5x}Mo_3O_{12}$ solid solution. *Chin. Phys. B* **2014**, *23*, 066501. [CrossRef]
124. Suzuki, T.; Omote, A. Negative Thermal Expansion in $HfMg(WO_4)_3$. *J. Am. Ceram. Soc.* **2004**, *87*, 1365–1367. [CrossRef]
125. Liu, Y.Y.; Yuan, B.H.; Cheng, Y.G.; Liang, E.J.; Ge, X.H.; Yuan, H.L.; Zhang, Y.; Guo, J.; Chao, M.J. Phase transition and negative thermal expansion of $HfMnMo_3O_{12}$. *Mater. Res. Bull.* **2018**, *99*, 255–259. [CrossRef]
126. Marinkovic, B.A.; Jardim, P.M.; Ari, M.; de Avillez, R.R.; Rizzo, F.; Ferreira, F.F. Low positive thermal expansion in $HfMgMo_3O_{12}$. *Phys. Status Solidi B* **2008**, *245*, 2514–2519. [CrossRef]
127. Miller, K.J.; Johnson, M.B.; White, M.A.; Marinkovic, B.A. Low-temperature investigations of the open-framework material $HfMgMo_3O_{12}$. *Solid State Commun.* **2012**, *152*, 1748–1752. [CrossRef]
128. Ge, X.H.; Mao, Y.C.; Li, L.; Li, L.P.; Yuan, N.; Cheng, Y.G.; Guo, J.; Chao, M.J.; Liang, E.J. Phase Transition and Negative Thermal Expansion Property of $ZrMnMo_3O_{12}$. *Chin. Phys. Lett.* **2016**, *33*, 046503. [CrossRef]
129. Li, T.; Liu, X.S.; Cheng, Y.G.; Ge, X.H.; Zhang, M.D.; Lian, H.; Zhang, Y.; Liang, E.J.; Li, Y.X. Zero and controllable thermal expansion in $HfMgMo_{3-x}W_xO_{12}$. *Chin. Phys. B* **2017**, *26*, 016501. [CrossRef]
130. Chen, D.X.; Yuan, B.H.; Cheng, Y.G.; Ge, X.H.; Jia, Y.; Liang, E.J.; Chao, M.J. Phase transition and near-zero thermal expansion in $ZrFeMo_2VO_{12}$. *Phys. Lett. A* **2016**, *380*, 4070–4074. [CrossRef]
131. Cheng, Y.G.; Liang, Y.; Mao, Y.C.; Ge, X.H.; Yuan, B.H.; Guo, J.; Chao, M.J.; Liang, E. A novel material of $HfScW_2PO_{12}$ with negative thermal expansion from 140 K to 1469 K and intense blue photoluminescence. *Mater. Res. Bull.* **2017**, *85*, 176–180. [CrossRef]
132. Ge, X.H.; Liu, X.S.; Cheng, Y.G.; Yuan, B.H.; Chen, D.X.; Chao, M.J.; Guo, J.; Wang, J.Q.; Liang, E.J. Negative thermal expansion and photoluminescence properties in a novel material $ZrScW_2PO_{12}$. *J. Appl. Phys.* **2016**, *120*. [CrossRef]
133. Ge, X.H.; Mao, Y.C.; Liu, X.S.; Cheng, Y.G.; Yuan, B.H.; Chao, M.J.; Liang, E.J. Negative thermal expansion and broad band photoluminescence in a novel material of $ZrScMo_2VO_{12}$. *Sci. Rep.* **2016**, *6*. [CrossRef] [PubMed]
134. Evans, J.S.O.; Mary, T.A.; Sleight, A.W. Structure of $Zr_2(WO_4)(PO_4)_2$ from powder X-ray data-cation ordering with no superstructure. *J. Solid State Chem.* **1995**, *120*, 101–104. [CrossRef]
135. Cetinkol, M.; Wilkinson, A.P. Pressure dependence of negative thermal expansion in $Zr_2(WO_4)(PO_4)_2$. *Solid State Commun.* **2009**, *149*, 421–424. [CrossRef]
136. Cetinkol, M.; Wilkinson, A.P.; Lee, P.L. Structural changes accompanying negative thermal expansion in $Zr_2(MoO_4)(PO_4)_2$. *J. Solid State Chem.* **2009**, *182*, 1304–1311. [CrossRef]
137. Baiz, T.I.; Gindhart, A.M.; Kraemer, S.K.; Lind, C. Synthesis of $MgHf(WO_4)_3$ and $MgZr(WO_4)_3$ using a non-hydrolytic sol-gel method. *J. Sol-Gel Sci. Technol.* **2008**, *47*, 128–130. [CrossRef]
138. Romao, C.P.; Perras, F.A.; Werner-Zwanziger, U.; Lussier, J.A.; Miller, K.J.; Calahoo, C.M.; Zwanziger, J.W.; Bieringer, M.; Marinkovic, B.A.; Bryce, D.L.; et al. Zero Thermal Expansion in $ZrMgMo_3O_{12}$: NMR Crystallography Reveals Origins of Thermoelastic Properties. *Chem. Mater.* **2015**, *27*, 2633–2646. [CrossRef]
139. Gindhart, A.M.; Lind, C.; Green, M. Polymorphism in the negative thermal expansion material magnesium hafnium tungstate. *J. Mater. Res.* **2008**, *23*, 210–213. [CrossRef]
140. Li, F.; Liu, X.S.; Song, W.B.; Yuan, B.H.; Cheng, Y.G.; Yuan, H.L.; Cheng, F.X.; Chao, M.J.; Liang, E.J. Phase transition, crystal water and low thermal expansion behavior of $Al_{2-2x}(ZrMg)_xW_3O_{12}\bullet n(H_2O)$. *J. Solid State Chem.* **2014**, *218*, 15–22. [CrossRef]
141. Zeng, G.J.; Yuan, H.L.; Guo, J.; Sun, Q.; Gao, Q.L.; Chao, M.J.; Ren, X.; Liang, E.J. Hydrate formation and its effects on the thermal expansion properties of $HfMgW_3O_{12}$. *Phys. Chem. Chem. Phys.* **2020**, *22*, 12605–12612. [CrossRef] [PubMed]
142. Omote, A.; Yotsuhashi, S.; Zenitani, Y.; Yamada, Y. High Ion Conductivity in $MgHf(WO_4)_3$ Solids with Ordered Structure: 1-D Alignments of Mg^{2+} and Hf^{4+} Ions. *J. Am. Ceram. Soc.* **2011**, *94*, 2285–2288. [CrossRef]

143. Madrid, A.; Ponton, P.I.; Garcia, F.; Johnson, M.B.; White, M.A.; Marinkovic, B.A. Solubility limit of Zn^{2+} in low thermal expansion $ZrMgMo_3O_{12}$ and its influence on phase transition temperature. *Ceram. Int.* **2020**, *46*, 3979–3983. [CrossRef]
144. Prisco, L.P.; Ponton, P.I.; Paraguassu, W.; Romao, C.P.; White, M.A.; Marinkovic, B.A. Near-zero thermal expansion and phase transition in $In_{0.5}(ZrMg)_{0.75}Mo_3O_{12}$. *J. Mater. Res.* **2016**, *31*, 3240–3248. [CrossRef]
145. Suzuki, T.; Omote, A. Zero thermal expansion in $(Al_{2x}(HfMg)_{1-x})(WO_4)_3$. *J. Am. Ceram. Soc.* **2006**, *89*, 691–693. [CrossRef]
146. Song, W.; Yuan, B.; Liu, X.; Li, Z.; Wang, J.; Liang, E. Tuning the monoclinic-to-orthorhombic phase transition temperature of $Fe_2Mo_3O_{12}$ by substitutional co-incorporation of Zr^{4+} and Mg^{2+}. *J. Mater. Res.* **2014**, *29*, 849–855. [CrossRef]
147. Miller, K.J.; Romao, C.P.; Bieringer, M.; Marinkovic, B.A.; Prisco, L.; White, M.A. Near-Zero Thermal Expansion in $In(HfMg)_{0.5}Mo_3O_{12}$. *J. Am. Ceram. Soc.* **2013**, *96*, 561–566. [CrossRef]
148. Cheng, Y.G.; Mao, Y.C.; Liu, X.S.; Yuan, B.H.; Chao, M.J.; Liang, E.J. Near-zero thermal expansion of $In_{2(1-x)}(HfMg)_xMo_3O_{12}$ with tailored phase transition. *Chin. Phys. B* **2016**, *25*, 086501. [CrossRef]
149. Cheng, Y.G.; Liang, Y.; Ge, X.H.; Liu, X.S.; Yuan, B.H.; Guo, J.; Chao, M.J.; Liang, E. A novel material of $HfScMo_2VO_{12}$ with negative thermal expansion and intense white-light emission. *RSC Adv.* **2016**, *6*, 53657–53661. [CrossRef]
150. Liang, Y.; Cheng, Y.G.; Ge, X.H.; Yuan, B.H.; Guo, J.; Sun, Q.; Liang, E.J. Negative thermal expansion and photoluminescence in solid solution $(HfSc)_{0.83}W_{2.25}P_{0.83}O_{12-\delta}$. *Chin. Phys. B* **2017**, *26*, 106501. [CrossRef]
151. Yuan, H.L.; Wang, C.Y.; Gao, Q.L.; Ge, X.H.; Sun, H.; Lapidus, S.H.; Guo, J.; Chao, M.J.; Jia, Y.; Liang, E.J. Structure and Negative Thermal Expansion in $Zr_{0.3}Sc_{1.7}Mo_{2.7}V_{0.3}O_{12}$. *Inorg. Chem.* **2020**, *59*, 4090–4095. [CrossRef]
152. Zhang, N.; Zhou, W.J.; Chao, M.J.; Mao, Y.C.; Guo, J.; Li, Y.X.; Feng, D.S.; Liang, E.J. Negative thermal expansion, optical and electrical properties of $HfMnMo_2PO_{12-\delta}$. *Ceram. Int.* **2015**, *41*, 15170–15175. [CrossRef]
153. Chen, D.X.; Yuan, B.H.; Yuan, H.L.; Ge, X.H.; Guo, J.; Liang, E.J.; Chao, M.J. Phase transition and thermal expansion properties of $Cr_{1.5-x}Sc_xZr_{0.5}Mo_{2.5}V_{0.5}O_{12}$. *Ceram. Int.* **2018**, *44*, 9609–9615. [CrossRef]
154. Ma, Q.; Chen, L.L.; Qi, H.; Xu, Q.; Yuan, B.H.; Liu, X.S.; Xu, L. Substitutions of Zr^{4+}/V^{5+} for Y^{3+}/Mo^{6+} in $Y_2Mo_3O_{12}$ for Less Hygroscopicity and Low Thermal Expansion Properties. *Materials* **2019**, *12*, 3945. [CrossRef] [PubMed]
155. Varga, T.; Wilkinson, A.P.; Lind, C.; Bassett, W.A.; Zha, C.-S. High pressure synchrotron X-ray powder diffraction study of $Sc_2Mo_3O_{12}$ and $Al_2W_3O_{12}$. *J. Phys. Condens. Matter* **2005**, *17*, 4271–4283. [CrossRef]
156. Varga, T.; Wilkinson, A.P.; Jorgensen, J.D.; Short, S. Neutron powder diffraction study of the orthorhombic to monoclinic transition in $Sc_2W_3O_{12}$ on compression. *Solid State Sci.* **2006**, *8*, 289–295. [CrossRef]
157. Torres Dias, A.C.; Luz Lima, C.; Paraguassu, W.; Pereira da Silva, K.; Freire, P.T.C.; Mendes Filho, J.; Marinkovic, B.A.; Miller, K.J.; White, M.A.; Souza Filho, A.G. Pressure-Induced Crystal-Amorphous Transformation In $Y_2Mo_3O_{12}$. *Vib. Spectrosc.* **2013**, *68*, 251–256. [CrossRef]
158. Baiz, T.I.; Heinrich, C.P.; Banek, N.A.; Vivekens, B.L.; Lind, C. In-situ non-ambient X-ray diffraction studies of indium tungstate. *J. Solid State Chem.* **2012**, *187*, 195–199. [CrossRef]
159. Liu, H.; Secco, R.A.; Imanaka, N.; Adachi, G. X-ray diffraction study of pressure-induced amorphization in $Lu_2(WO_4)_3$. *Solid State Commun.* **2002**, *121*, 177–180. [CrossRef]
160. Garg, N.; Murli, C.; Tyagi, A.K.; Sharma, S.M. Phase transitions in $Sc_2(WO_4)_3$ under high pressure. *Phys. Rev. B* **2005**, *72*, 064106. [CrossRef]
161. Cetinkol, M.; Wilkinson, A.P.; Lind, C. In situ high-pressure synchrotron X-ray diffraction study of $Zr_2(WO_4)(PO_4)_2$ up to 16 GPa. *Phys. Rev. B* **2009**, *79*, 224118. [CrossRef]
162. Young, L.; Gadient, J.; Lind, C. High Pressure Behavior of Chromium and Yttrium Molybdate ($Cr_2Mo_3O_{12}$, $Y_2Mo_3O_{12}$). *Front. Chem.* **2018**, *6*. [CrossRef] [PubMed]
163. Secco, R.A.; Liu, H.; Imanaka, N.; Adachi, G.; Rutter, M.D. Electrical conductivity and amorphization of $Sc_2(WO_4)_3$ at high pressures and temperatures. *J. Phys. Chem. Solids* **2002**, *63*, 425–431. [CrossRef]
164. Secco, R.A.; Liu, H.; Imanaka, N.; Adachi, G. Anomalous ionic conductivity of $Sc_2(WO_4)_3$ mediated by structural changes at high pressures and temperatures. *J. Phys. Condens. Matter* **2002**, *14*, 11285–11289. [CrossRef]
165. Mukherjee, G.D.; Vijaykumar, V.; Achary, S.N.; Tyagi, A.K.; Godwal, B.K. Phase transitions in $Al_2(WO_4)_3$: High pressure investigations of low frequency dielectric constant and crystal structure. *J. Phys. Condens. Matter* **2004**, *16*, 7321–7330. [CrossRef]
166. Karmakar, S.; Deb, S.K.; Tyagi, A.K.; Sharma, S.M. Pressure-induced amorphization in $Y_2(WO_4)_3$: In situ X-ray diffraction and Raman studies. *J. Solid State Chem.* **2004**, *177*, 4087–4092. [CrossRef]
167. Young, L.; Gadient, J.; Xiaodong, G.; Lind, C. High pressure studies of $A_2Mo_3O_{12}$ negative thermal expansion materials (A_2 = Al_2, Fe_2, FeAl, AlGa). *J. Solid State Chem.* **2016**, *237*, 121–128. [CrossRef]
168. Tran, K.D.; Groshens, T.J.; Nelson, J.G. Fabrication of near-zero thermal expansion $(Fe_xSc_{1-x})_2Mo_3O_{12}$-$MoO_3$ ceramic composite using the reaction sintering process. *Mater. Sci. Eng. A* **2001**, *303*, 234–240. [CrossRef]
169. Yanase, I.; Miyagi, M.; Kobayashi, H. Fabrication of zero-thermal-expansion $ZrSiO_4/Y_2W_3O_{12}$ sintered body. *J. Eur. Ceram. Soc.* **2009**, *29*, 3129–3134. [CrossRef]
170. Xiao, X.; Zhou, W.J.; Liu, X.S.; Chao, M.J.; Li, Y.C.; Zhang, N.; Liu, Y.M.; Li, Y.X.; Feng, D.S.; Liang, E.J. Electrical properties of Al-$ZrMgMo_3O_{12}$ with controllable thermal expansion. *Ceram. Int.* **2015**, *41*, 2361–2366. [CrossRef]
171. Liu, X.S.; Cheng, F.X.; Wang, J.Q.; Song, W.B.; Yuan, B.H.; Liang, E.J. The control of thermal expansion and impedance of Al-$Zr_2(WO_4)(PO_4)_2$ nano-cermets for near-zero-strain Al alloy and fine electrical components. *J. Alloys Compd.* **2013**, *553*, 1–7. [CrossRef]

172. Yanase, I.; Sakai, H.; Kobayashi, H. Fabrication of $Zr_2WP_2O_{12}/ZrV_{0.6}P_{1.4}O_7$ composite with a nearly zero-thermal-expansion property. *Mater. Lett.* **2017**, *207*, 221–224. [CrossRef]
173. Liu, H.F.; Sun, W.K.; Xie, X.; Yang, L.; Zhang, Z.P.; Zhou, M.; Zeng, X.H.; Chen, X.B. Adjustable Thermal Expansion Properties in $Zr_2MoP_2O_{12}/ZrO_2$ Ceramic Composites. *Front. Chem.* **2018**, *6*. [CrossRef] [PubMed]
174. Zhang, Z.P.; Sun, W.K.; Liu, H.F.; Xie, G.; Chen, X.B.; Zeng, X.H. Synthesis of $Zr_2WP_2O_{12}/ZrO_2$ Composites with Adjustable Thermal Expansion. *Front. Chem.* **2017**, *5*. [CrossRef] [PubMed]
175. Liu, Q.Q.; Fan, C.Y.; Wu, G.D.; Zhao, Y.H.; Sun, X.J.; Cheng, X.N.; Shen, J.T.; Hu, Y.M. In-situ synthesis of $Sc_2W_3O_{12}$/YSZ ceramic composites with controllable thermal expansion. *Ceram. Int.* **2015**, *41*, 8267–8271. [CrossRef]
176. Wu, M.M.; Zu, Y.; Peng, J.; Liu, R.D.; Hu, Z.B.; Liu, Y.T.; Chen, D.F. Controllable thermal expansion properties of $In_{2-x}Cr_xMo_3O_{12}$. *Cryst. Res. Technol.* **2012**, *47*, 793–798. [CrossRef]
177. Cheng, Y.Z.; Sun, X.Y.; Xiao, X.L.; Liu, X.F.; Xue, L.; Hu, Z.B. Effects of doping Fe cations on crystal structure and thermal expansion property of $Yb_2Mo_3O_{12}$. *Chin. Chem. Lett.* **2017**, *28*, 1600–1606. [CrossRef]
178. Cheng, Y.G.; Mao, Y.C.; Yuan, B.H.; Ge, X.H.; Guo, J.A.; Chao, M.J.; Liang, E.J. Enhanced negative thermal expansion and optical absorption of $In_{0.6}(HfMg)_{0.7}Mo_3O_{12}$ with oxygen vacancies. *Phys. Lett. A* **2017**, *381*, 2195–2199. [CrossRef]
179. Liu, X.S.; Ge, X.H.; Liang, E.J.; Zhang, W.F. Effects of Al particles and thin layer on thermal expansion and conductivity of Al-$Y_2Mo_3O_{12}$ cermets. *Chin. Phys. B* **2017**, *26*, 118101. [CrossRef]
180. Yang, J.R.; Wang, L.; Tan, X.R.; Zhi, Q.; Yang, R.B.; Zhang, G.P.; Liu, Z.X.; Ge, X.H.; Liang, E.J. Effect of sintering temperature on the thermal expansion behavior of $ZrMgMo_3O_{12}$p/2024Al composite. *Ceram. Int.* **2018**, *44*, 10744–10752. [CrossRef]
181. Kohler, J.; Imanaka, N.; Adachi, G.Y. New cation conducting solid electrolytes with the $Sc_2(WO_4)_3$ type structure. *J. Mater. Chem.* **1999**, *9*, 1357–1362. [CrossRef]
182. Imanaka, N. Novel multivalent cation conducting ceramics and their application. *J. Ceram. Soc. Jpn.* **2005**, *113*, 387–393. [CrossRef]
183. Zhou, Y.K.; Adams, S.; Rao, R.P.; Edwards, D.D.; Neiman, A.; Pestereva, N. Charge Transport by Polyatomic Anion Diffusion in $SC_2(WO_4)_3$. *Chem. Mater.* **2008**, *20*, 6335–6345. [CrossRef]
184. Arfaoui, A.; Mhamdi, A.; Jlidi, D.; Belgacem, S. Physical and ethanol sensing properties of sprayed $Fe_2(MoO_4)_3$ thin films. *J. Alloys Compd.* **2017**, *719*, 392–400. [CrossRef]
185. Grissa, R.; Martinez, H.; Pele, V.; Cotte, S.; Pecquenard, B.; Le Cras, F. An X-ray photoelectron spectroscopy study of the electrochemical behaviour of iron molybdate thin films in lithium and sodium cells. *J. Power Sources* **2017**, *342*, 796–807. [CrossRef]
186. Heo, J.W.; Hyoung, J.; Hong, S.T. Unveiling the Intercalation Mechanism in $Fe_2(MoO_4)_3$ as an Electrode Material for Na-Ion Batteries by Structural Determination. *Inorg. Chem.* **2018**, *57*, 11901–11908. [CrossRef] [PubMed]
187. Huu, H.T.; Im, W.B. Facile Green Synthesis of Pseudocapacitance-Contributed Ultrahigh Capacity $Fe_2(MoO_4)_3$ as an Anode for Lithium-Ion Batteries. *ACS Appl. Mater. Interfaces* **2020**, *12*, 35152–35163. [CrossRef]
188. Lin, Z.D.; Xu, M.Y.; Fu, P.; Deng, Q.R. Crystal plane control of 3D iron molybdate and the facet effect on gas sensing performances. *Sens. Actuators B Chem.* **2018**, *254*, 755–762. [CrossRef]
189. Nguyen, V.; Liu, Y.L.; Yang, X.; Chenz, W. $Fe_2(MoO_4)_3$/Nanosilver Composite as a Cathode for Sodium-Ion Batteries. *ECS Electrochem. Lett.* **2015**, *4*, A29–A32. [CrossRef]
190. Niu, Y.B.; Xu, M.W. Reduced graphene oxide and $Fe_2(MoO_4)_3$ composite for sodium-ion batteries cathode with improved performance. *J. Alloys Compd.* **2016**, *674*, 392–398. [CrossRef]
191. Zhang, F.H.; Wang, Y.C.; Wang, L.; Liu, J.; Ge, H.L.; Wang, B.; Huang, X.Y.; Wang, X.D.; Chi, Z.T.; Xie, W.F. High performance $In_2(MoO_4)_3$@In_2O_3 nanocomposites gas sensor with long-term stability. *J. Alloys Compd.* **2019**, *805*, 180–188. [CrossRef]